Aggregate

WILEY

Aggregate

RESEARCH ARTICLE OPEN ACCESS

Engineering "Meso-Atom" Bonding: Honeycomb-Network Transitions in Reticular Liquid Crystals

Christian Anders[1] | Tianyi Tan[2] | Virginia-Marie Fischer[3] | Ruoyu Wang[2] | Mohamed Alaasar[1] | Rebecca Waldecker[3] | Yu Cao[2] | Feng Liu[2] | Carsten Tschierske[1]

[1]Institute of Chemistry, Martin-Luther University Halle-Wittenberg, Halle, Germany | [2]Shannxi International Research Center for Soft Matter, State Key Laboratory for Mechanical Behavior of Materials, Xi'an Jiaotong University, Xi'an, China | [3]Institute of Mathematics, Martin-Luther University Halle-Wittenberg, Halle, Germany

Correspondence: Yu Cao (yu.cao@xjtu.edu.cn) | Carsten Tschierske (carsten.tschierske@chemie.uni-halle.de)

Received: 12 October 2024 | **Revised:** 26 November 2024 | **Accepted:** 7 December 2024

Funding: This research was financially supported by the Deutsche Forschungsgemeinschaft (Grant 436494874), National Natural Science Foundation of China (Grant 12204369), Science and Technology Agency of Shaanxi (Grant 2023-YBGY-459), and China Postdoctoral Science Foundation (Grants 2022M712551 and 2023T160505).

ABSTRACT

A library of rod-like bolapolyphiles with sticky hydrogen-bonded glycerol groups at their ends and having highly branched side chains with a carbosilane-based four-way branching point, all based on the same oligo(phenylene ethynylene) core, has been synthesized and investigated. For these compounds, a A15-type Frank–Kasper phase is formed upon side-chain elongation in the steric frustration range at the transition from the triangular to the much larger square honeycombs. In contrast to the previously known tetrahedral sphere packings the A15 phase is in this case formed by tetrahedral networks of aggregates of parallelly organized π-conjugated rods. This allows the design of compounds with wide ranges of the A15 network down to room temperature. However, its formation becomes strongly disfavored by core fluorination that is attributed to a changing mode of core–core interaction that also modifies the square honeycombs by deformation of the squares into rectangular or rhombic cells, either with or without emergence of tilt of the rods.

1 | Introduction

The aggregation of π-conjugated molecules into well-defined structures and their precise programmed arrangement in space represents a contemporary challenge of importance for numerous applications such as photovoltaics [1], induced and polarized emission [2–6], and the design of light harvesting systems [7, 8]. Liquid crystals (LCs) combining rigid polyaromatic units with flexible chains provide the possibility to organize such π-conjugated units into ordered arrays under thermodynamic control in a bottom-up approach [9–12]. In addition, the mobility of the molecules in these LC phases allows easy manipulation of the local and macroscopic structures by external stimuli, as, for example, used in display technology [13]. Previous LCs were found to form relatively simple structures such as nematic phases [14], layers, and columns, mainly depending on the shape of the aromatic core structure. More complex superstructures—allowing more sophisticated future applications of LCs [15]—were achieved by polyphilic molecules [16] among them the so-called bolapolyphiles [17–19]. These bolapolyphiles represent molecules combining a rigid polyaromatic rod with more than just two incompatible segments, while "bola" [20] means molecules having highly polar groups at both ends of a less polar central unit. In our case, this unit is a rod-like

---

Christian Anders and Tianyi Tan contributed equally to this study.

Aggregate, 2025; 6:e728
https://doi.org/10.1002/agt2.728

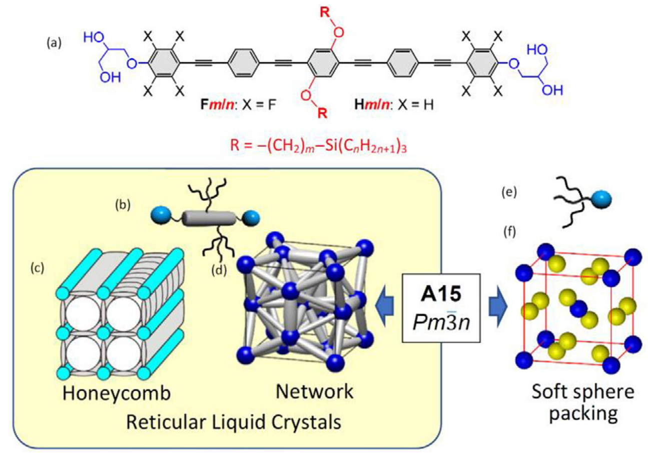

FIGURE 1 | (a) Structure and nomenclature of compounds **H*m*/*n*** and **F*m*/*n*** with the side chains shown in red. The first letter H or F indicates molecules with nonfluorinated OPE or semiperfluorinated FOPE core, respectively, while the combination *m*/*n* indicates the length *m* of the alkylene spacer connecting the (F)OPE core with the Si branching points in the side chains, and *n* is the length of the three alkyl chains attached to Si. (b) A schematic sketch of the considered bolapolyphiles. (c, d) The phase structures; reticular LC can be divided into (c) honeycombs and (d) 3D networks that can both be described within the meso-atom concept as outlined in [87]; (c) shows a square honeycombs and (d) the segmented FK-type tetrahedral network with $Pm\bar{3}n$ space group. (e) A dendritic amphiphile known to form (f) the $Pm\bar{3}n$ sphere packing without interconnecting junctions (blue and yellow indicate the crystallographic different positions of the spheres).

π-conjugated system, and polar glycerol groups at both ends provide cooperative and dynamic hydrogen bondings [21–24] between them, giving rise to end-to-end attractions (rods with sticky ends,[25, 26], see, e.g., Figure 1b). However, the naturally preferred parallel alignment of the long rods is distorted by the attached flexible side chains, giving rise to various new states of aggregation. Typically, in these LC phases, the polyaromatic cores aggregate into ribbons of parallelly organized rods which are interconnected at the junctions by strings of the H-bonding networks of the glycerols to honeycombs with their polygonal cells filled by the flexible side chains (Figure 1c) [17, 18, 27, 28]. The shape of the honeycomb cells can be modified in a wide range from triangular via square (Figure 1c) and pentagonal to hexagonal, including those with nonregular shapes [29, 30] and mixtures of different types of polygonal cells [31, 32].

For larger side chains, the number of polyaromatic rods forming the ribbons becomes limited, leading to a splitting into rod-bundles. These smaller aggregates of polyaromatic rod-bundles form struts with the glycerols at the junctions interconnecting them into 3D-networks [33–37]. Among them, the recently discovered tetrahedral network with $Pm\bar{3}n$ space group is a unique structure (Figure 1d) [38] due to its close relationship with Frank–Kasper-type (FK) sphere packings [39–42], specifically, the A15 phase (Figure 1f). Huge efforts have been made to design and investigate the A15 sphere packing in solid-state modifications of metals, alloys and intermetallic compounds [43], in aqueous lyotropic systems [44–47], in the soft mesophases of different types of amphiphilic [48–50], and dendritic molecules [47–78], as well as in block copolymer morphologies [79–83], and to understand their formation under the aspect of minimizing the interfaces in soft sphere packings (Figure 1g,h) [84–86]. However, in the new type of FK phase formed by polyphiles the focus is on the engineering of the struts interconnecting the spherical aggregates at the junctions. In this case, the spheres at the junctions can be considered as a kind of “superatoms” [86] or “meso-atoms” [87–89] that are interconnected by bonds between them (“meso-atom” bonds) [90].

Here we report about engineering of meso-atom bonding in such reticular (net-like) [91] LCs. For this purpose, we use bolapolyphiles with oligo(phenylene ethynylene) (OPE) [92] rods and sticky ends having two highly branched carbosilane-based side chains with the silicon acting as a tetravalent branching point in these chains [93, 94]. The side-chain effects, as well as the effects of core fluorination [95] on the aggregation of the OPE rods [27, 30, 38, 96–100] into different reticular LC, either into honeycombs, or alternatively, into network structures (Figure 1c,d) are investigated. In these compounds, X*m*/*n* (Figure 1a) X = H means a nonfluorinated OPE core and X = F indicates an FOPE core with perfluorinated benzene rings at both peripheries, besides the glycerol groups. The numbers *m*/*n* give the aliphatic spacer length *m* and the alkyl chain length *n* in each branch, respectively (Figure 1a). In a previous short communication, we have reported the effect of spacer length *m* at constant chain length on the LC phase formation for a series of compounds with fixed $n = 7$ [94]. Here, we provide a much wider study of a larger library of OPE-based bolapolyphiles depending on the side-chain volume, side-chain length, and core-fluorination in order to fully understand their soft self-assembly, especially the conditions for A15 phase formation in the perspective of polyaromatic core aggregation. It is found that the A15 FK-type network phase represents an intermediate structure in the frustration range at the transition between triangular and square honeycombs (mainly determined by the side-chain length and volume), but only if an easy longitudinal shift between the individual polyaromatic rods can take place. Any restriction of this shift by specific core–core interactions removes the A15 phase that is then replaced by different types of deformed honeycombs.

2 | Experimental

2.1 | Materials

All compounds were synthesized as shown in Figure 2 by Sonogashira coupling [101] of the 2,5-dialkylated 1,4-diiodobenzenes **4/*m*/*n*** with the acetylene terminated building blocks **5H** or **5F** [27, 99, 100]. For compounds with spacer lengths $m = 4$–12, the carbosilane chains were attached by alkylation of diiodohydroquinone with the bromosubstituted carbosilanes **2/*m*/*n***, while for compounds with $m = 3$, 1,4-diallyloxybenzene was hydrosilylated [102] with the *H*-carbosilanes **1/*n*** [103] and then iodinated with a hypervalent iodination reagent [104] to yield the diiodohydroquinone ethers **4/3/*n***. The bromosubstituted carbosilanes **2/*m*/*n*** were prepared by hydrosilylation of ω-bromoalkenes with **1/*n*** and in the final step the glycerol groups of the bisacetonides of **H*m*/*n*** and **F*m*/*n*** (**H*m*/*n*A** and **H*m*/*n*A**), they were deprotected under mild acidolytic conditions using pyridinium *p*-toluene sulfonate (PPTS) [105] to give the final compounds that were purified by repeated column chromatography. The experimental

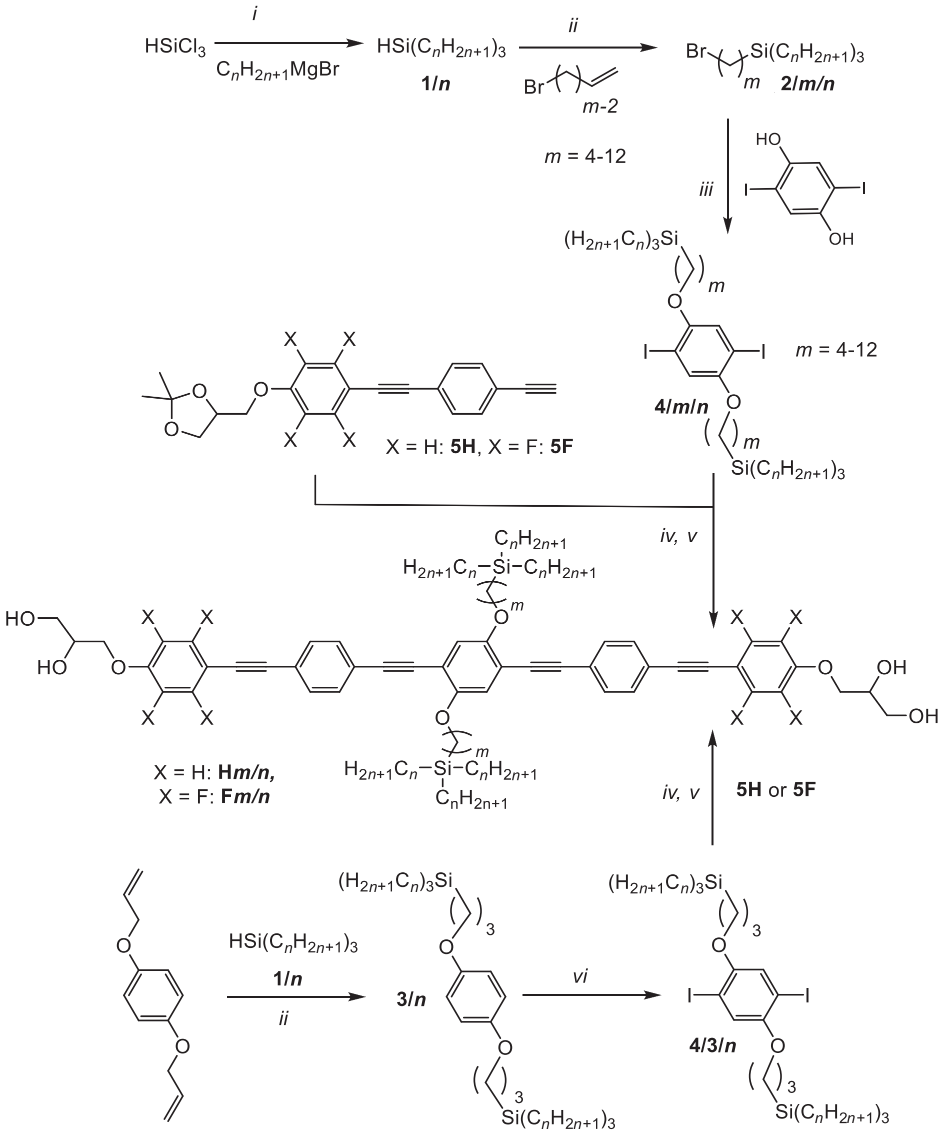

FIGURE 2 | Synthesis of compounds **H*m*/*n*** and **F*m*/*n***. *Reagents and conditions*: (i) THF, LiCl, 20°C, 24 h; (ii) CH$_2$Cl$_2$, Karstedts cat., 20°C, 1 day; (iii) K$_2$CO$_3$, Bu$_4$NI, DMF, 80°C, 3 days; (iv) Pd(PPh$_3$)$_4$, CuI, Et$_3$N, 80°C, 1 day; (v) PPTS, MeOH/THF, 50°C; (vi) PhI(OCOCF$_3$)$_2$, I$_2$, DCM, 60°C, 1 day.

details and the analytical data and details of the synthesis of the ethynyltolanes **5H** and **5F** are provided in the Synthesis Section of Supporting Information.

3 | Methods

Investigation of the compounds was performed by differential scanning calorimetry (DSC), polarizing optical microscopy (POM), small- and wide-angle X-ray scattering (SAXS and WAXS) and UV-Vis and fluorescence measurements in thin films under the conditions and with the equipment described in the methods section in the Supporting Information.

4 | Results and Discussion

4.1 | Series of Nonfluorinated Compounds H*m*/*n*

Three different reticular LC phases, namely, Col$_{hex}$/$p6mm$, Cub$_{net}$/$Pm\bar{3}n$, and Col$_{squ}$/$p4mm$, were identified (Table 1). Two of them form birefringent spherulite- and fan-like textures between crossed polarizers (Figure 3a–f) as typical for columnar LC phases (Col). POM Investigation with an additional λ-retarder plate (Figure 3d) show negative birefringence by the blue shift of the fans along the slow indicatrix axis, meaning that the major conjugation pathway of the π-conjugated rods lays perpendicular to the column long axis, as typical for honeycomb LC phases. In contrast, the cubic phase (Cub$_{net}$) is optically isotropic and can be distinguished from the isotropic liquid only by the significantly higher viscosity and the presence of sharp scatterings in the SAXS patterns. In addition, the Cub–Iso transition is associated with a small DSC peak (0.3–1.8 kJ mol^{-1}, see Table 1 and Figure 3g).

The WAXS patterns of the columnar and cubic mesophases of compounds **H*m*/*n*** are diffuse with a single maximum around 0.45–0.46 nm (Figure 3h), indicating the absence of positional order between individual molecules and thus confirming the LC state. The SAXS patterns of the birefringent colmnar phases can be indexed either to a hexagonal $p6mm$ lattice (ratio of reciprocal d-spacing is $1:\sqrt{3}:2:\sqrt{7}\ldots$; see Figure 4a) or to a square

TABLE 1 | LC phases, transition temperatures, transition enthalpies, and lattice parameters of compounds **H*m*/*n***.[a]

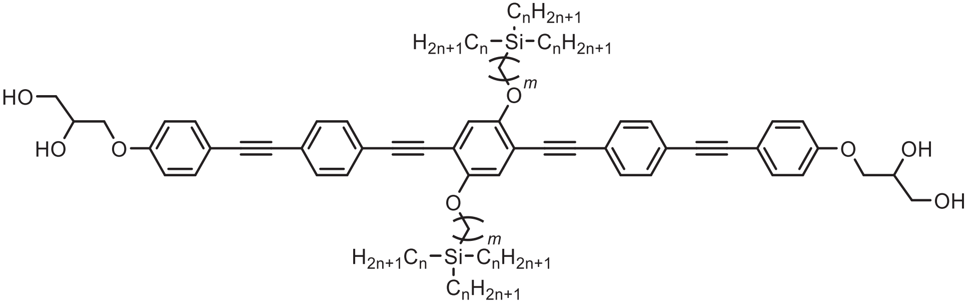

Compound	***m***	***n***	***T*/°C [Δ*H*/kJ mol^{-1}]**	***a*/nm@*T*/°C**	**V_C**	**L_C**
H3/6	3	6	Cr 93 [24.1] *p6mm* 163 [5.0] Iso	4.27@130	44	10
H3/7[b]	3	7	Cr 70 [13.6] *p6mm* 147 [3.5] $Pm\bar{3}n$ 160 [1.5] Iso	4.39@101 8.62@151	50	11
H6/6	6	6	Cr 59 [31.3] *p6mm* 108 [2.8] $Pm\bar{3}n$ 155 [1.6] Iso	4.38@69 9.09@119		13
H4/7[b]	4	7	Cr 91 [41.5] $Pm\bar{3}n$ 159 [1.3] Iso	8.89@119	52	12
H8/6	8	6	Cr 67 [23.4] M 109 [2.2] $Pm\bar{3}n$ 139 [0.5] Iso	9.13@119	54	15
H3/8	3	8	Cr 75 [14.6] *p6mm* 120 [4.4] $Pm\bar{3}n$ 162 [1.8] Iso	4.45@69 4.29@110 8.84@120	56	12
H6/7[b]	6	7	Cr 54 [16.3] M 85 [1.1] $Pm\bar{3}n$ 146 [0.5] Iso	9.19@92		14
H9/6	9	6	Cr 87 [18.3] *p4mm* 118 [3.3] Iso	4.14@96		16
H4/8	4	8	Cr 74 [29.5] $Pm\bar{3}n$ 157 [1.8] Iso	8.85@110	58	13
H5/8	5	8	Cr 74 [24.0] M 104 [4.5] $Pm\bar{3}n$ 157 [1.6] Iso	9.06@119	60	14
H8/7[b]	8	7	Cr 45 [1.5] *p4mm* 105 [3.0] $Pm\bar{3}n$ 128 [0.4] Iso	4.12@64 9.13@105		16
H11/6	11	6	Cr 85 [17.2] *p4mm* 142 [5.2] Iso	4.54@120		18
H3/9	3	9	Cr 67 [19.8] *p6mm* 101 [4.3] $Pm\bar{3}n$ 157 [1.8] Iso	4.44@74 8.89@110	62	13
H6/8	6	8	Cr 68 [13.1] $Pm\bar{3}n$ 147 [0.8] Iso	9.15@101		15
H9/7[b]	9	7	Cr 80 [11.1] *p4mm* 127 [4.0] Iso	4.16@101 3.93@121		17
H4/9	4	9	Cr 50 [23.7] $Pm\bar{3}n$ 155 [2.1] Iso	8.86@119	64	14
H10/7[b]	10	7	Cr 83 [11.1] *p4mm* 134 [5.4] Iso	4.18@110		18
H11/7[b]	11	7	Cr 78 [11.8] *p4mm* 142 [5.4] Iso	4.25@92	66	19
H3/10	3	10	Cr 88 [53.4] $Pm\bar{3}n$ 156 [2.2] Iso	8.81@128	68	14
H6/9	6	9	Cr 59 [28.5] *p4mm* 64 [-] $Pm\bar{3}n$ 128 [0.3] Iso	3.99@54 9.01@101		16
H4/10	4	10	Cr 55 [14.7] $Pm\bar{3}n$ 146 [1.7] Iso	8.98@101	70	15

Note: Ordered according to growing V_C values and for identical V_C with growing spacer length *m*.

Abbreviations: Cr, crystalline solid (in the case of different crystalline modifications only the highest melting one is given here); Iso, isotropic liquid; L_C, number of C and Si atoms along each side-chain between ether oxygen and most distant end, L_C, $m + n + 1$; M, unknown birefringent mesophases; *p4mm*, square honeycomb (Col_{squ}/*p4mm*); *p6mm*, triangular honeycomb (Col_{hex}/*p6mm*); $Pm\bar{3}n$, cubic network phase with $Pm\bar{3}n$ space group ($Cub_{net}/Pm\bar{3}n$, for model see Figure 1d); V_C, total number of C and Si atoms in both side chains, V_C, $2(m + 3n + 1)$; for data on cooling, see Figure 5 and Table S1; for DSC traces, see Figure S1; additional structural data can be found in Tables S31-S33.

[a] Peak temperatures as determined by DSC (10 K min^{-1}) on cooling.

[b] See [94].

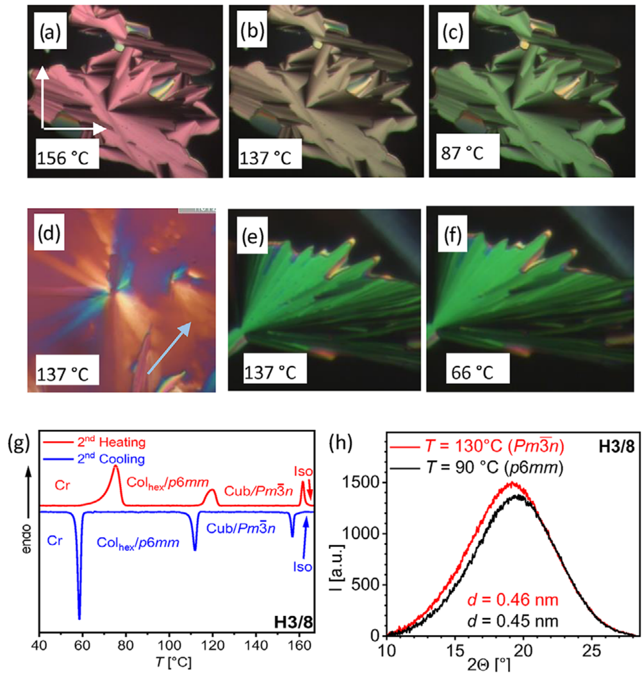

FIGURE 3 | (a–c) Textures of the $\mathrm{Col_{hex}}/p6mm$ phase of **H3/6** as observed between crossed polarizers (arrows in (a)) on cooling at the given temperatures; the changing color of the fan-like domains shows the decreasing Δn. (d–f) Textures of the $\mathrm{Col_{squ}}/p4mm$ phase of **H11/6**, (d) shows the texture with λ-retarder plate, indicating negative Δn (blue shift along the indicatrix slow axis indicated by the arrow); dark areas in (a–c) and (e, f) are homeotropic aligned areas with the columns perpendicular to the substrates. (g) DSC traces and (h) WAXS scans of **H3/8**.

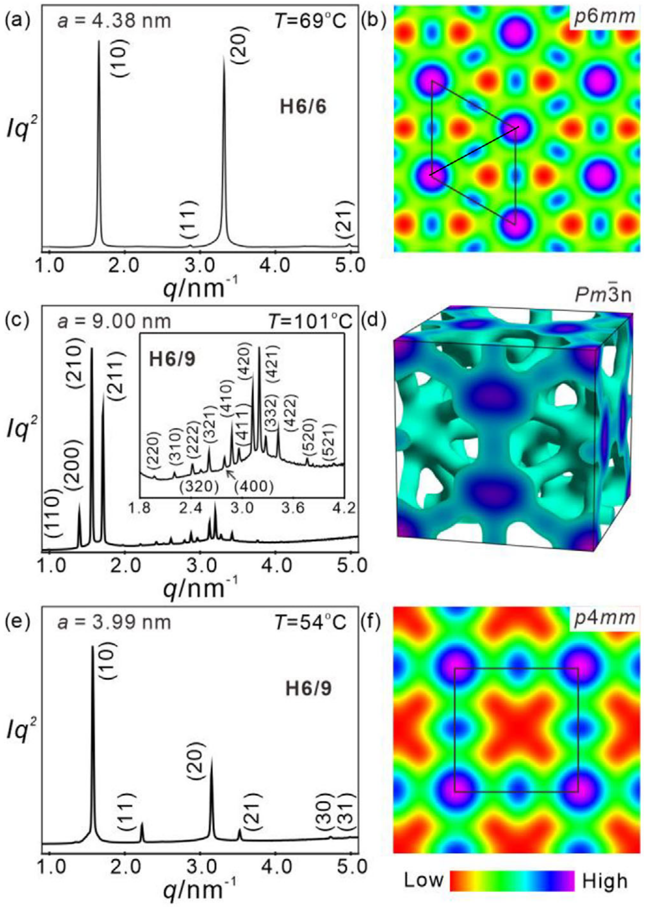

FIGURE 4 | SAXS patterns of compounds **H*m*/*n*** with a nonfluorinated OPE core: (a, c, e) SAXS patterns, (b, d, f) the corresponding ED maps, (a, b) in the $\mathrm{Col_{hex}}/p6mm$ phase of **H6/6** at 69°C (triangular honeycomb), (c, d) in the $\mathrm{Cub_{net}}/Pm\bar{3}n$ phase of compound **H6/9** at 101°C (A15 phase), (e, f) in the $\mathrm{Col_{squ}}/p4mm$ phase of **H6/9** at 54°C (square honeycomb); in (b, f) the positions of the OPE rods in one unit cells are shown as black lines, for a model of (d), see Figure 1d; for additional SAXS patterns and ED maps, see Figures S6 and S8; the origin of the enhanced intensity of the (20) reflection in the columnar phases is explained in Figure S8b.

*p*4*mm* lattice (ratio of reciprocal *d*-spacing is $1{:}\sqrt{2}{:}2, \ldots$, see Figure 4e). The triangular and square honeycomb structures of the LC phases are confirmed by the reconstructed electron density (ED) maps (see Figure 4b,f), where the red areas represent the low-ED centers of the columns, formed by the alkyl side chains filling the polygonal prismatic cells (triangular or square, respectively). These are enclosed by the OPE cores as sides and the high-ED polar glycerol groups (blue/purple) as junctions of the honeycomb cells. The light blue high-ED dots in the middle of the honeycomb walls are due to the two electron-rich ether oxygens connecting the side chains to the middle benzene rings. The lattice parameter in the $\mathrm{Col_{hex}}$ phases is $a_{\mathrm{hex}} = 4.2$–4.5 nm (Table S31) that is close to the maximum value of the molecular length (L_{mol}) as measured between the ends of the glycerol groups ($L_{\mathrm{mol}} = 4.0$–4.4 nm) and typical for triangular honeycombs [27]. Likewise, the lattice parameters of the square phase ($a_{\mathrm{squ}} = 3.9$–4.5 nm; Table S33) are in line with a square honeycomb, though there is a wider variation of a_{squ} depending on side-chain volume. There is also a temperature dependence of the lattice parameter in both phases which is, however, small (<0.1 nm in the phase ranges, see Figure S9). The number of molecules organized side-by-side in the lateral cross-section of the honeycomb walls (n_{wall}) is around 0.9–1.1 (“single molecule walls”) in the triangular and a bit larger, around 1.2–1.7 (shifted toward “double molecule walls”) in the square honeycombs (these are no integer numbers due to molecular staggering and molecular dynamics in the LC state; see Tables S31 and S33). This difference is due to the different valence (ν) of the junctions connecting the cylinder walls, being $\nu = 6$ in $\mathrm{Col_{hex}}$ and only $\nu = 4$ in $\mathrm{Col_{squ}}$. Due to the larger valence of the junctions, the cross-section of the polar glycerol columns would be larger in the triangular honeycombs. However, this difference is compensated by the tendency of the polar columns to retain their diameter in a narrow range and this requires an increase of n_{wall} in the square honeycomb. Thus, in both honeycomb phases, the diameter of the polar columns remains in the range between 4.8 and 6.6 glycerols in the cross-section. These limits appear to be the result of two competing forces. On one hand, the columns are stabilized by increasing the number of cooperative (polarization enhanced) and dynamic H-bonding interactions between the glycerols [21–24], providing a tendency for lattice-expansion, while on the other hand, the limited size of the polar glycerol units restricts the possible column expansion without distorting nano-segregation by significant overlapping of lipophilic OPE cores and polar glycerols upon shifting the molecules with respect to each other. Outside this range, the honeycombs become instable and are replaced by other modes of self-assembly.

The absence of a temperature dependence of the birefringence (see Figure 3e,f), and a larger variation of n_{wall} in the square honeycombs indicates that adjustment of the cell volume to the space actually required by the side-chain volume (depending on m, n, and T) is in this case mainly achieved by lattice shrinkage/expansion due to variation of n_{wall}. In contrast, in the triangular honeycombs, the variation in n_{wall} is much smaller and a decrease of birefringence with rising temperature is observed (color change from green, via reddish green to red see textures of **H3/6** in Figure 3a–c). This means that in this case, the main contribution to the adjustment of cell volume and chain volume is provided by a changing orientational-order parameter of the rods in the walls (random tilt of the rods in the walls), that is, due to a changing of the effective molecular length. It seems that the relatively long spacer units in the molecules forming the square honeycombs allows an easy adjustment of n_{wall}, which is more difficult for the triangular honeycombs, mainly formed by molecules having shorter spacers, where the bulky —SiR_3 groups close to the core reduce their capability of forming double molecular walls. Hence, long spacers allow an easy compensation of differences between prismatic cell volume and effective chain volume by changing n_{wall}. However, this becomes more difficult as the spacer length is reduced, and in this case a change of the orientational-order parameter or tilting of the rods is required to adjust the cell size. It is noted that the change of the orientational-order parameter and tilt are also affected by the core–core interactions as discussed further below for compounds **F*m*/*n***.

Most investigated compounds **H*m*/*n*** form a cubic mesophase above one of the honeycomb phases or even as the only observable mesophase. The SAXS patterns show three strong reflections that can be indexed to (200), (210), and (211) reflections of a lattice with $Pm\bar{3}n$ space group (Figure 4c). All the remaining weaker reflections can be indexed to this space group, too. The ED map indicates a packing of high-ED spheres at the corners, in the center and as pairs of spheres on the faces of the unit cell of the cubic lattice, as typical for the A15 phase (Figure 4d). Moreover, the high-ED glycerol spheroids are interconnected by a tetrahedral network of medium-ED bonds, indicating struts formed by bundles of parallel OPE rods (see also Figure 1d). The low-ED alkyl chains, filling the continuum around them, are omitted for clarity. In these segmented networks there are two different types of spheroids with different valence (12 + 14), size, and shape, requiring that also the bond lengths are different and assume the values $0.5a_{\mathrm{cub}}$, $0.56a_{\mathrm{cub}}$, and $0.61a_{\mathrm{cub}}$ [38]. The lattice parameters are $a_{\mathrm{cub}} = 8.6$–9.2 nm from which the length of the bonds can be calculated to be $L_{\mathrm{bond}} = 4.3$–5.5 nm. This length exceeds that of the individual molecules **H*m*/*n*** and this is attributed to the significant size of the glycerol spheroids interconnecting 12- and 14 rod-bundles, respectively. The number of molecules per unit cell is between 240 and 320 ($n_{\mathrm{cell,LC}}$, see Table S32) which are distributed among the 54 bonds interconnecting the spheroids, meaning that there are on average 4.4–5.9 molecules organized side-by-side in the bundles of parallelly aligned OPEs. This number decreases with growing n and tends to increase with elongation of m (Table S32). A number of about 53–71 glycerols is organized in the smaller spheroids with $\nu = 12$ ($V_{\mathrm{sph}} = 6.5$–8.7 nm^3, as estimated using Immirzi's crystal volume increments [106]) in the center and at the corners, whereas the larger spheroids with $\nu = 14$ on the faces of the unit cell are each formed by 62–83 glycerols ($V_{\mathrm{sph}} = 7.6$–10.1 nm^3). Assuming a spherical shape, their diameters would be 2.3–2.6 and 2.4–2.7 nm, respectively. Considering $L_{\mathrm{OPE\text{-}core}} = 3.1$ nm, the distance between the centers of the spheres should be 5.4–5.8 nm, being just around the upper limit of the bond length of 5.5 nm. This indicates some intercalation of OPE cores and glycerols requiring some longitudinal shift between the OPE cores (see discussion of **F*m*/*n*** further below).

The overall sequence of phases is affected by the side-chain volume V_{C}, calculated from the total number of C and Si atoms in both side chains as $V_{\mathrm{C}} = 2(m + 3n + 1)$. This leads to the sequence Col$_{\mathrm{hex}}$/$p6mm$ ($V_{\mathrm{C}} = 44$–50) → Cub$_{\mathrm{net}}$/$Pm\bar{3}n$ ($V_{\mathrm{C}} = 50$–70) → Col$_{\mathrm{squ}}$/$p4mm$ ($V_{\mathrm{C}} = 60$–70). However, as obvious from Table 1, this sequence is not strict, there are several cases for which the observed phases do not follow this rule, as for example, the Col$_{\mathrm{hex}}$ phases of **H3/8** with $V_{\mathrm{C}} = 56$ and **H3/9** with $V_{\mathrm{C}} = 62$ occur for much larger side-chain volumes, while the Col$_{\mathrm{squ}}$ phase of **H9/6** with $V_{\mathrm{C}} = 56$ is found for a smaller volume than expected. If one compares the three compounds with constant chain volume $V_{\mathrm{C}} = 56$, the sequence Col$_{\mathrm{squ}}$/$p6mm$ → Cub$_{\mathrm{net}}$/$Pm\bar{3}n$ → Col$_{\mathrm{hex}}$/$p4mm$ is observed for growing spacer lenght from **H3/8** via **H6/7** to **H9/6**. The same sequence is found for the series of compounds **H3/9**, **H6/8**, and **H9/7** with $V_{\mathrm{C}} = 62$. This means that at identical V_{C} long spacers prefer the square honeycomb and short spacers the triangular honeycombs, and the cubic $Pm\bar{3}n$ phase is found as the intermediate structure at the transition between them. Both series occur upon increasing the spacer length (m) while simultaneously decreasing the length of the three alkyl branches (n) to keep the total chain volume V_{C} constant. This means that it is not sufficient that the chain volume fits with the cell volume, but the chains must also be sufficiently long to efficiently fill the most distant spaces in the selected structure. Increasing the spacer length m contributes more to an increase of the total $L_{\mathrm{C}} = m + n + 1$, while increasing the length of the three branches (n) contributes mostly to V_{C} and less to L_{C}. Ordering the compounds **H*m*/*n*** according to the side-chain length L_{C}, and for identical side-chain length according to growing spacer length m, as shown in the bar diagram in Figure 5, provides a much clearer picture showing a transition Col$_{\mathrm{squ}}$/$p6mm$ → Cub$_{\mathrm{net}}$/$Pm\bar{3}n$ → Col$_{\mathrm{squ}}$/$p4mm$ with growing side-chain length L_{C}. In the series **H*m*/*n***, the $Pm\bar{3}n$ phase becomes the dominating phase for compounds with relatively short spacers ($m \sim 3$–8) and medium length of the branches ($n \sim 8$–9), overall having a total side-chain length range from $L_{\mathrm{C}} = 11$ to 16, corresponding to $L_{\mathrm{chain}} = 1.5$ to 2.1 nm.

The dV/dr curves in Figure 6 support the observed phase sequence. For each curve, the intersection with the x-axis refers to the furthest distance required to fill the lattice, and the area occupied by the curves represents the volume requirement for each molecule. The shape of the curves provides information about the development of the chain volume depending on the distance from the core (r). The $Pm\bar{3}n$ phase (blue) requires short side-chain length (r), large side-chain volume (given as areas V/r in Figure 6), and a strong volume increase (dV/dr) close to the OPE core that is provided by the compounds **H*m*/*n*** with short spacers m and longer n, while the formation of the triangular honeycomb (red) is favored for molecules with limited side-chain volume and a smaller increase of dV/dr. However, as shown in

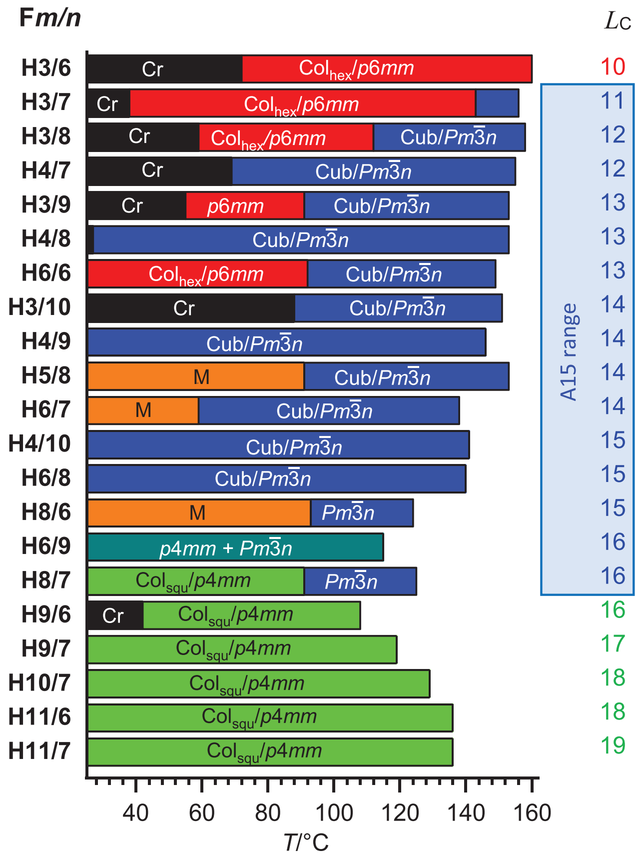

FIGURE 5 | Bar diagram of series **Hm/n** ordered according to increasing $L_C = m + n + 1$ and for identical L_C with growing number of CH_2 units (m) in the spacer. The temperatures were recorded on cooling with 10 K min^{-1}.

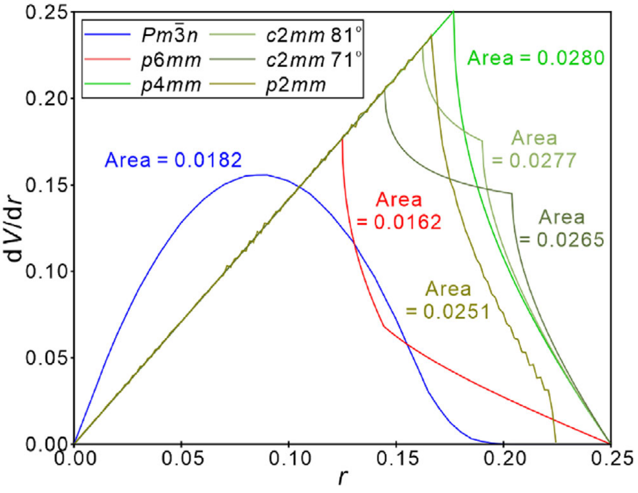

FIGURE 6 | dV/dr curve of the LC phases formed by **Hm/n** and **Fm/n**. The aromatic core length is taken as 0.5 to normalize all phases. The given area values are the areas under the curves as a measure of the total chain volume. The calculation of the curves is described in the Supporting Information.

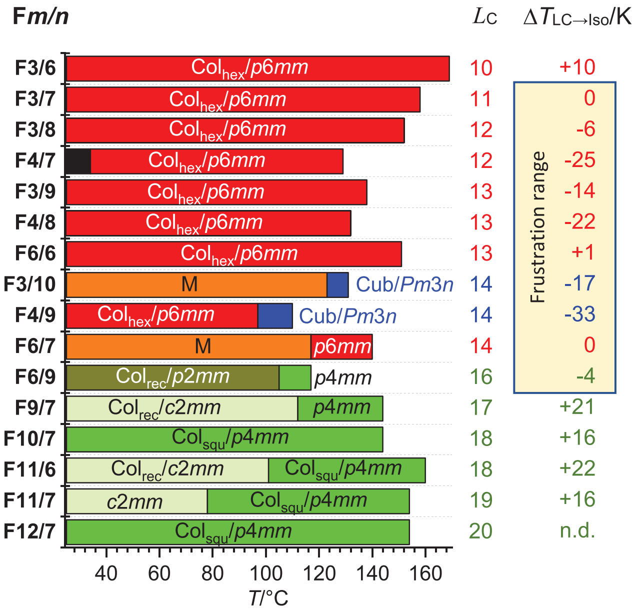

FIGURE 7 | Bar diagram of series **Fm/n** ordered according to increasing side-chain length L_C and growing m, and showing the LC phases and their transitions as observed on *cooling* with 10 K min^{-1}; at the right the differences between the LC → Iso transition temperatures: $\Delta T_{LC\rightarrow Iso} = T_{LC\rightarrow Iso}$ (**Fm/n**)—$T_{LC\rightarrow Iso}$ (**Hm/n**) based on the data on *heating* (Tables S1 and S2) with 10 K min^{-1}; for abbreviations, see Tables 1 and 2.

Figure 6, the curves of *p6mm* and *Pm*3̄*n* cross each other and the areas occupied are close, thus both structures can compete with each other and the majority of the *Pm*3̄*n* phase occurs close to the *p6mm* phase (Figure 5). There is a transition *p6mm*-*Pm*3̄*n*-*p4mm* with growing spacer length *m*, and for any *m*, larger *n* favors *Pm*3̄*n* due to larger chain volume and more possibilities of chain folding. On top of this, there appears to be an odd–even effect. A bent-shaped odd-numbered $m + 1$ (1 stands for the ether oxygen) contributes to a steeper dV/dr growth, favoring *Pm*3̄*n* more than a related linear even numbered. In all cases with *p6mm*-*Pm*3̄*n* dimorphism, higher chain flexibility supports chain folding and thus additionally favors *Pm*3̄*n* at high temperature above *p6mm*. Moreover, the increased possibilities of chain orientations and conformations makes the *Pm*3̄*n* phase also entropically more favorable. Further increasing *m* favors *p4mm* (green line in Figure 6; the other yellowish green lines are explained further below).

4.2 | Honeycomb vs. Network Competition in the Series of Fluorinated Compounds Fm/n

In a next step, a series of related core-fluorinated compounds **Fm/n** with almost the same chain volume range (V_C = 44–68) was investigated (Table 2; Figure 7), where clear trends can also be identified. First of all, the probability of finding the *Pm*3̄*n* phase is dramatically reduced by core fluorination. The existence range of the *p6mm* phase is significantly expanded and among the

TABLE 2 | LC phases, transition temperatures transition enthalpies, and lattice parameters of compounds **F*m*/*n***.[a]

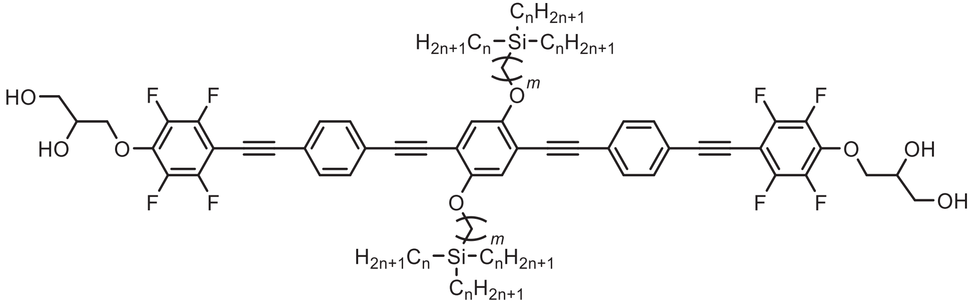

F*m*/*n*	***m***	***n***	T/°C [ΔH/kJ mol^{-1}]	***a*,*b*/nm @*T*/°C**	V_C	L_C
F3/6	3	6	Cr 41 [3.3] *p6mm* 173 [11.1] Iso	4.48@83	44	10
F3/7[b]	3	7	Cr 44 [2.8] *p6mm* 160 [6.3] Iso	4.43@120	50	11
F6/6	6	6	Cr < 20 *p6mm* 156 [5.3] Iso	4.51@151		13
F4/7[b]	4	7	Cr 50 [9.2] *p6mm* 134 [2.8] Iso	4.29@64	52	12
F3/8	3	8	Cr 39 [5.9] *p6mm* 156 [8.9] Iso	4.35@115	56	12
F6/7[b]	6	7	Cr < 20 M 131 [0.3] *p6mm* 146 [5.4] Iso	4.30@92		14
F4/8	4	8	Cr 30 [6.9] *p6mm* 135 [4.9] Iso	4.33@83	58	13
F11/6	11	6	Cr 74 [8.4] *c2mm* 115 [-] *p4mm* 164 [11.1] Iso	*a* = 5.14; *b* = 6.82@78 4.24@124	60	18
F3/9	3	9	Cr 37 [7.8] M 105 [0.9] *p6mm* 143 [4.5] Iso	4.43@55	62	13
F9/7[b]	9	7	Cr 59 [8.2] *c2mm* 115 [-] *p4mm* 148 [8.8] Iso	*a* = 4.92; *b* = 6.92@60 4.14@119		17
F4/9	4	9	Cr 64 [1.8] *p6mm* 103 [2.6] $Pm\bar{3}n$ 122 [0.5] Iso	4.30@74 8.98@101	64	14
F10/7[b]	10	7	Cr 94 [22.0] *p4mm* 150 [4.8] Iso	4.14@74		18
F11/7[b]	11	7	Cr 67 [10.2] *c2mm* 80 [-] *p4mm* 158 [9.1] Iso	*a* = 5.25; *b* = 6.64 @46 4.26@119	66	19
F3/10	3	10	Cr 105 [3.3] M1 118 [0.8] M2 129 [6.8] $Pm\bar{3}n$ 139 [1.1] Iso	8.70@136	68	14
F6/9	6	9	Cr < 20 *p2mm* 108 [1.5] *p4mm* 124 [6.6] Iso	*a* = 4.16; *b* = 3.64@92 4.00@105		16
F12/7[b]	12	7	Cr 94 [18.5] *p4mm* 159 [10.8] Iso	4.23@137		20

Note: For data on cooling, see Figure 5 and Table S1; for DSC traces, see Figure S2; additional structural data can be found in Tables S31–S33.

Abbreviations: *c2mm*, rhombic honeycomb (Col$_{rec}$/*c2mm*); *p2mm*, rectangular honeycomb (Col$_{rec}$/*p2mm*); M1, M2, different unknown birefringent mesophases; for all other abbreviations, see Table 1.

[a] Ordered according to growing V_C values and for identical V_C with growing spacer length *m*. Peak temperatures as determined by DSC (10 K min^{-1}) on heating.

[b] See [94].

investigated compounds, there are only two compounds with L_C = 14 (**F3/10** and **F4/9**) with a small $Pm\bar{3}n$ range of about 10–20 K. However, even in this case, the Cub–Iso transition temperature is reduced strongly by 17 and 33 K in comparison with the nonfluorinated compounds **H3/10** and **H4/9**, respectively. Thus, the molecular structural space for $Pm\bar{3}n$ phase formation is much narrower and the stability of this phase is considerably reduced by core fluorination. In contrast, there appears to be a general stabilizing core-fluorination effect for the honeycomb phases (Figure 7) that overcompensates the steric distortion of core packing provided by fluorination [95, 107, 108]. This effect, giving rise to a mesophase stabilization by about 10–20 K upon core-fluorination is only observed for compounds with optimal space filling in the prismatic cells (L_C < 11 for *p6mm* and L_C > 16 for *p4mm*, see Figure 7). All compounds between these limits, experience some steric frustration leading in most cases to a decrease of the LC → Iso transition temperature by up to 33 K upon fluorination (see frustration range in Figure 7).

The SAXS patterns of the *p6mm*, *p4mm*, and $Pm\bar{3}n$ phases of compounds **F*m*/*n*** indicate lattice parameters in the ranges of a_{hex} = 4.2–4.5 nm, a_{squ} = 4.0–4.3 nm, and a_{cub} = 8.7–9.0 nm, being almost identical with those of compounds **H*m*/*n*** (compare Figures 4a,c,e and 8a,c,e). Hence, their phase structures are almost identical and there is no recognizable effect of core fluorination on these parameters (for a discussion of the textures,

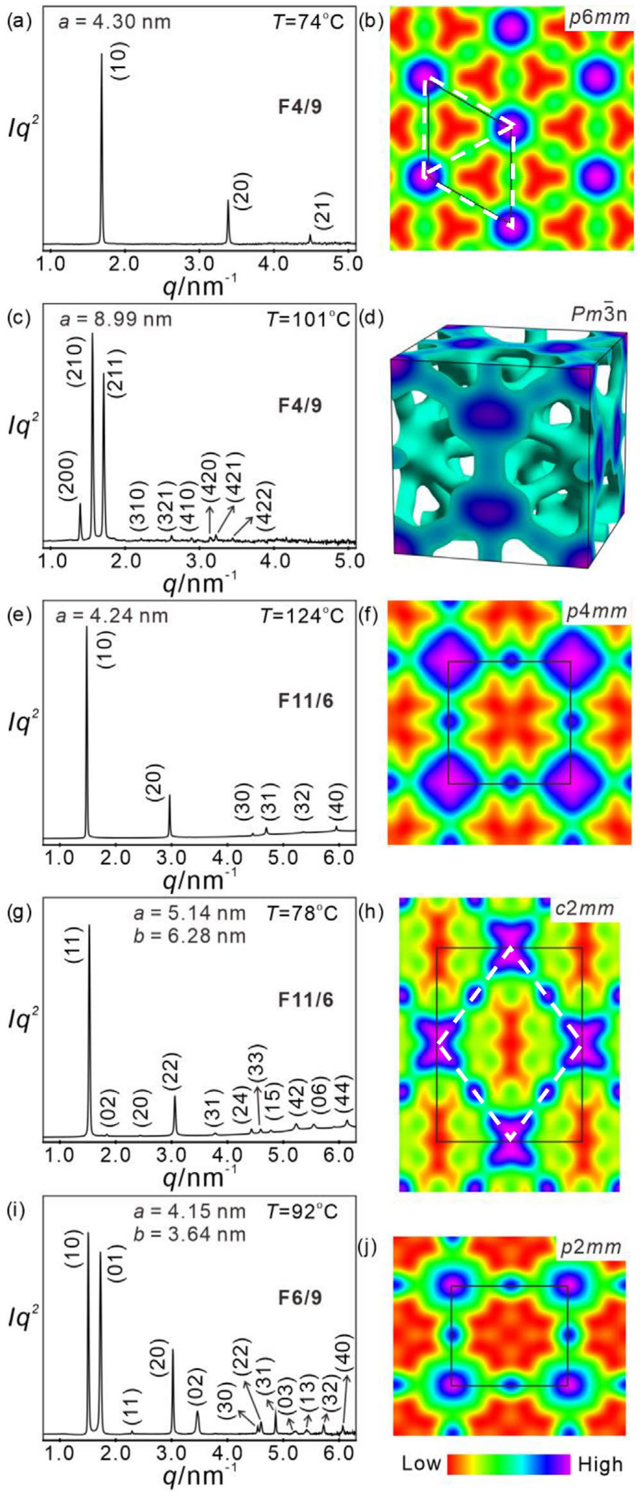

FIGURE 8 | SAXS patterns (left) and ED maps (right) of representative compounds **F*m*/*n*** in their mesophases. The black lines indicate the unit cells, which coincide with the honeycomb cells, except for (b) and (h) where the honeycomb cells are indicated by the white dotted lines; for additional SAXS patterns and ED maps, see Figures S7 and S8a.

see Figure S3). Slight differences in the ED maps are caused by differences in the intensity distribution of the reflections compared to **H*m*/*n*** due to the enhanced ED of the perfluorinated ends of the FOPE cores (see Figure 8b,d,f).

A major difference between the series **H*m*/*n*** and **F*m*/*n*** is found in the WAXS patterns (Figure 9). For most core fluorinated compounds there is an additional weak shoulder around $d = 0.36$–0.38 nm besides the main diffuse scattering, being absent for the nonfluorinated compounds (Figure 3h). We attribute it to a contribution of closer face-to-face stacking interactions between neighboring FOPE cores, while for the electron-rich OPE compounds **H*m*/*n***, the larger core–core distance around 0.45 nm (in the WAXS overlapping with the mean alkyl chain distances, see Figure 3h) allows an almost free rotation around the rod long axes. Thus, the OPE cores can assume different stacking modes, including face-to-face [109] and edge-to-face arrangements [110]. In the series of compounds **F*m*/*n***, the contribution of the shoulder around 0.36–0.38 nm increases with growing spacer length *m* (Figure 9), because longer spacers allow a closer packing of the FOPE cores, while short spacers lead to a significant disturbance of face-to-face core packing by the bulky R_3Si units in closer proximity. For the *p6mm* phases of the compounds with short spacers, this steric suppression of π-stacking is especially pronounced (Figure 9a,b). The relative intensity of the shoulder increases with lowering temperature (Figure 9a,c,d), indicating an improved packing, in line with the growing-order parameter (Figure S3a,b). The very diffuse character of this shoulder indicates only a short coherence length of this stacking over only a few molecules, in line with the significant molecular dynamics in the LC phases. It is not visible in the $Pm\bar{3}n$ phase range of **F4/9** and **F3/10** (Figures 9b and S5d) because of the limited length of π-stacking in the rod-bundles.

UV-Vis absorption and emission spectra were recorded for representative compounds in the *p6mm* and $Pm\bar{3}n$ phases of compounds **H3/9** and **F4/9**, as shown in Figure 10. For the absorption spectra of **H3/9** (Figure 10a), two main absorptions centered around 338 and 388 nm at low temperature can be assigned as the HOMO$_2$ to LUMO and HOMO to LUMO transitions of the OPE core (Figure S12) [111]. Upon heating, a minor red shift of 10–15 nm can be found for the two main absorptions, which is attributed to an increasing intramolecular twist along the OPE core. However, only a minor difference between **H3/9** and **F4/9** can be found in the absorption spectra. Compound **F4/9** mainly exhibits a blue shift of ~15 nm compared with **H3/9** that is attributed to the effects of fluorination on the frontier orbitals energy. A striking feature of the **H3/9** emission spectra (Figure 10c) is that it emits around 480 nm and a minor blue shift (~10 nm) can be found upon heating up to the cubic phase. **F4/9** gives a very different feature with emission around 510 nm and a stronger blue shift (~20 nm) upon heating (Figure 10d). Such difference can be attributed to the effect of aggregation. For OPEs, there are two types of planarization due to aggregation. One is from loose packing (aggregation-induced coplanarization) and another one is from ordered packing (cofacial planar aggregation) (Figure S13) [112]. The more ordered packing induces red shift of the emission as well as extension of stokes shift due to stronger intermolecular π–π interaction. This further supports the improved planarization and denser packing of the FOPEs compared with the OPEs. Overall, the OPE cores assume a loose aggregation in the LC range, whose planar conformation gradually turns into more twisted conformation upon heating. FOPE with stronger intermolecular interaction has reduced twist and stacks into more ordered packing.

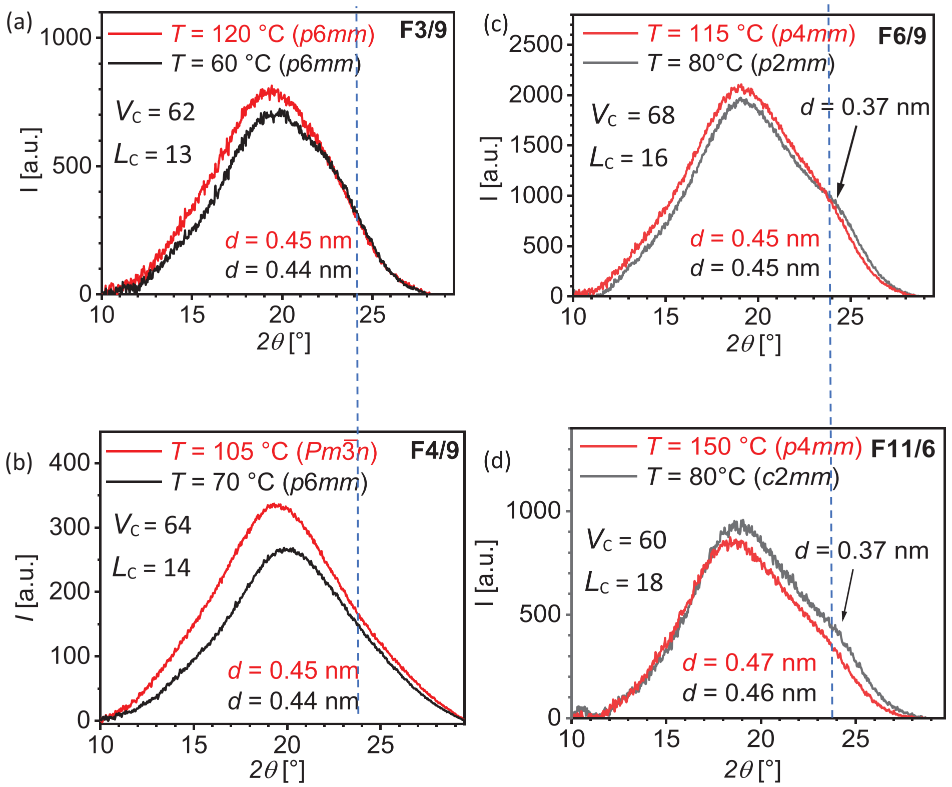

FIGURE 9 | WAXS patterns of compounds ***Fm/n*** depending on the V_C and L_C values, in the different LC phases and depending on spacer length. The dash line indicates the peak position of π–π stacking around 0.37 nm; for more WAXS patterns, see Figures S4 and S5.

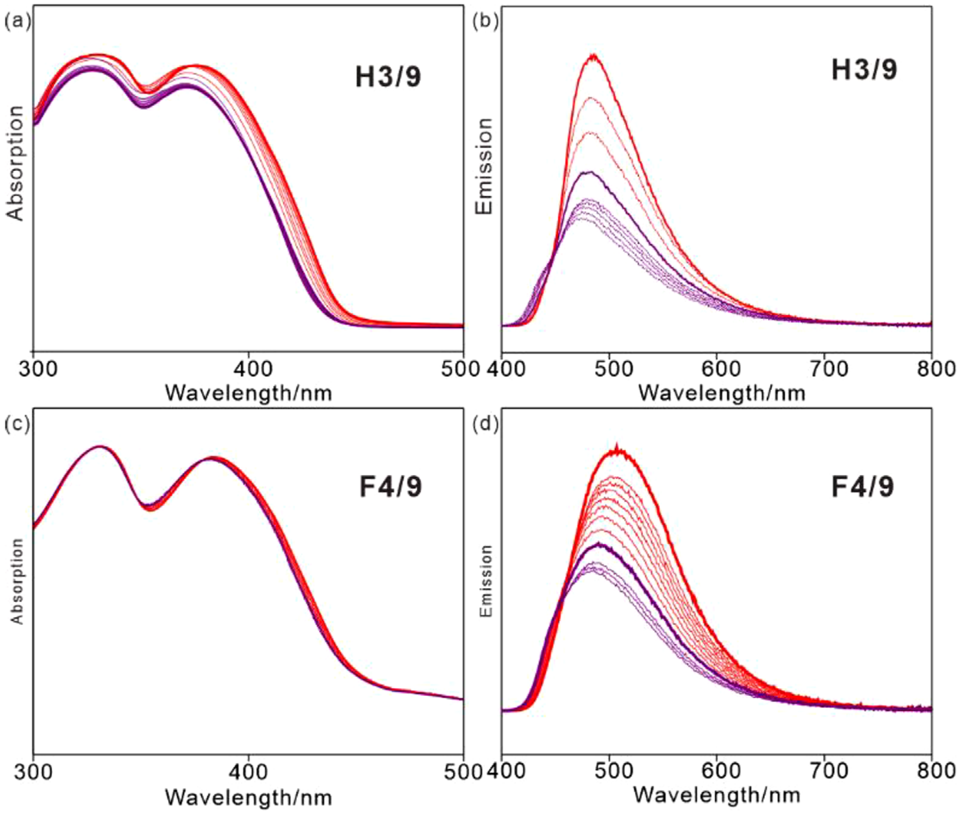

FIGURE 10 | UV-Vis absorption and emission spectra of (a, b) **H3/9**; (c, d) **F4/9**. Color code: red: *p6mm*; purple: *Pm*$\bar{3}$*n*; the thick lines indicate the phase transition temperatures; for additional examples, see Figure S10.

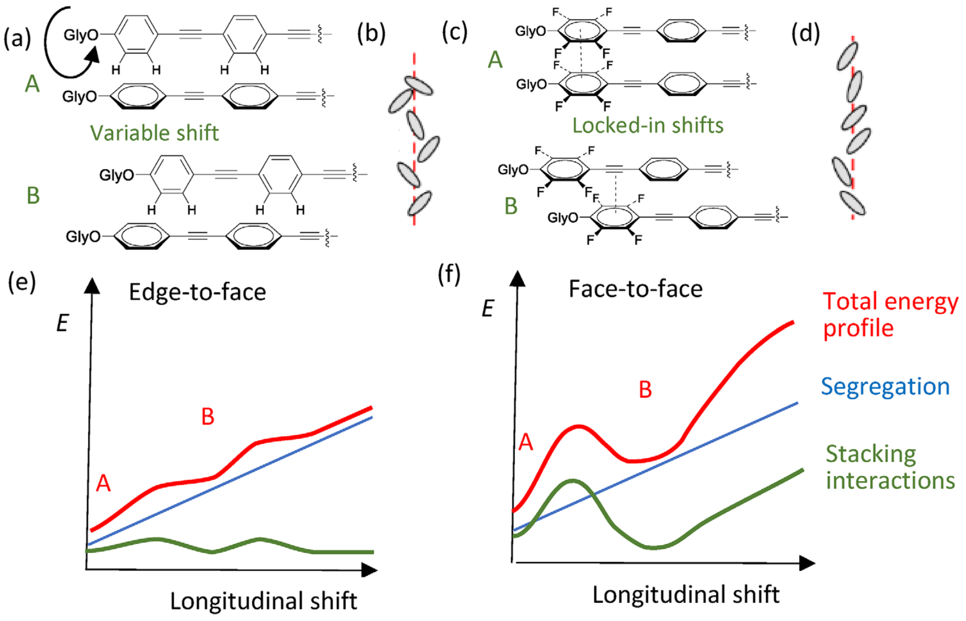

FIGURE 11 | (a–d) Schematics of the rod-packing, and (e, f) sketches of their tentative energy profiles depending on longitudinal shift (a–d) views on the packing of the rods in the honeycombs (a, c) view along a short axis (only the two outer rings at one end of the molecules are shown) and (b, d) side-views along the long axes of the rod-like (F)OPE cores, and (e, f) the effects of stacking interactions and glycerol-(F)OPE segregation on the energy profiles of the longitudinal shift between neighboring molecules; (a, b, e) there is an easy longitudinal sliding of the rotationally less ordered nonfluorinated OPE cores due to larger core–core distances (only edge-to-face packing is shown although also face-to-face and other arrangements contribute) and twisted conformations must be considered, while (c, d, f) for the FOPEs the reduced twist allows a denser packing with distinct preferred longitudinal shifts for the distinct face-to-face stacking motifs. Gly = glycerol end groups.

This explains the stabilization of the triangular (+10 K) and especially the square honeycomb (+20 K) by core fluorination, observed as long as the side-chain volume fits with the prismatic cell volume and these chains have the appropriate length to reach the centers of the cells (Figure 7). The non-shifted side-by-side packing of the electron-deficit perfluorinated rings in these honeycombs (Figure 11c(A)) requires some lateral offset of the interacting rings (tangential shift), leading to some out-of-plane twist of the benzene rings to optimize the face-to-face interaction (Figure 11d) [113–116]. As the coherence length of the twist direction is only short the scattering corresponding to the π-stacking distance is broad and weak (Figure 9).

In the region with intermediate side-chain length L_C (Figure 7), there is a frustration between the spaces and distances provided by the honeycomb framework with fixed side lengths and the volumes and lengths of the side chains, which leads to a reduced stability of the triangular and square honeycombs, thus allowing alternative modes of self-assembly to take place. For most of them, the honeycombs are retained albeit with reduced LC-Iso transition temperature (frustration range in Figure 7). This means that due to the stronger core–core interactions the spitting of the honeycombs into a network of rod-bundles becomes disfavored. Nevertheless, if compared with compounds ***Hm/n***, the limited phase range and phase stability of the $Pm\bar{3}n$ phase in the series ***Fm/n*** is surprising. We attribute the easier formation of the $Pm\bar{3}n$ network in the case of the series ***Hm/n*** to the larger lateral stacking distance of the OPE cores of compounds ***Hm/n***, allowing an easy and nonrestricted longitudinal shift of adjacent OPE cores (Figure 11a,e). In contrast, the shorter stacking distance and a preference for face-to-face stacking of the ***Fm/n*** compounds provides more pronounced energetic minima and maxima for the longitudinal shift (Figure 11c,f) [117]. There is a minimum for the side-by-side packing of the electron-deficit perfluorinated benzenes without longitudinal shift as noted above, and a second minimum for the significant shift required for the donor–acceptor packing of the fluorinated benzenes besides the π-electron–rich acetylene [118, 119] or benzene units of adjacent molecules (Figure 11c(B)) [120–126]. In the $Pm\bar{3}n$ network, there are different lengths for the strut bonds connecting the polar glycerol spheroids, requiring a length ratio 1:1.12:1.22 that is achieved by deformation of the spheres to spheroids and by some longitudinal shifting of the polyaromatic rod in the bundles to modify the bond length. In the case of compounds ***Hm/n*** with wider lateral distances between the OPEs, a slight shift of neighboring OPEs with respect to one another is easily possible, and thus, the length of the rod-bundles can be precisely adjusted to the required distances. However, for the FOPE cores with a significant contribution of closer face-to-face stacking, there are distinct preferred values of the shift which do not fit with the required values, and this provides an energetic penalty for $Pm\bar{3}n$ formation. Due to this mismatch and the small correlation length of the rods in the bundles of the A15 phase ($n_{\text{bundle}} = 4.1$ for **F3/10** and 4.8 for **F4/9**, Table S32), face-to-face stacking is difficult to develop and therefore cannot contribute to network stabilization, in line with the absence of a shoulder in the WAXS patterns (Figures 9b and S5d). Hence, $Pm\bar{3}n$ phase stability is reduced by core-fluorination, and in most cases, the competing honeycomb phases are preserved.

4.3 | Honeycomb Deformation in the Series of Fluorinated Compounds F*m*/*n*

Finally, we focus on the deformed square honeycomb phases (*p*2*mm* and *c*2*mm*) induced by core fluorination (Table 2; Figure 7). One possible mode of deformation is the angular deformation of the square to a rhombic honeycomb as observed for the low temperature $\mathrm{Col}_{\mathrm{rec}}/c2mm$ phase of compounds **F11/6**, **F9/7** and **F11/7** with side lengths corresponding to the full molecular length and inner angle of 71°–81° (for SAXS patterns and ED maps, see Figure 8g,h). It is found for compounds with long odd-numbered m ($m = 9, 11$), that is, overall even-numbered spacers ($m + 1$) considering the ether oxygen. Under the polarizing microscope, the transition from *p*4*mm* to *c*2*mm* is detected by the emergence of biaxiality in the homeotropically aligned areas and a slight increase of Δn of the spherulitic domains (Figure S3e,f), the first confirms the onset of phase biaxiality and the latter indicating some improvement of the orientational-order parameter of the rods in the honeycomb walls during the square to rhomb transition. The rhombic honeycomb is removed for compounds with even number m (i.e., odd-numbered $m + 1$; **F10/7, F12/7**) [94] and its stability is reduced as the side-chain length n is increased. The latter is due to the improved space filling in the square cells of long chain compounds, thus reducing the driving force of cell deformation. Hence, there is a preference of rhombic cells for molecules with a linear even-numbered spacer $m + 1$, while for bent odd-numbered $m + 1$, formation of square cells is supported. It is assumed that the spacer linearity allows a denser parallel chain packing in the rhombic cells, while more disordered chains prefer the square cells with higher symmetry.

For compound **F6/9**, the molecule with the shortest spacer length m and smallest L_{C} among the *p*4*mm* phase forming compounds, being located at the transition to the smaller triangular honeycomb, another mode of prismatic cell deformation is observed (Figure 8i,j). In this case, retaining the 90° angles but modifying the length of two opposite sides of the square honeycomb leads to a $p4mm \rightarrow p2mm$ transition on cooling. The parameter $a_{\mathrm{rec}} = 4.15$ is in the range of L_{mol}, while $b_{\mathrm{rec}} = 3.64$ nm (at $T = 92°\mathrm{C}$) is significantly shorter. There are two different possible types of this kind of transition. The first is based on the elliptical deformation of the glycerol columns without tilting, giving rise to a lattice shrinkage in one and a similar expansion in the orthogonal direction, as previously observed for molecules with relatively short core units (e.g., *p*-terphenyl) [127, 128]. The second type is caused by the emergence of a tilt in two opposite sides of the square cells [129]. In the case of **F6/9**, the length of two opposite sides is almost retained, while only the two sides in the orthogonal direction shrink significantly. The transition *p*4*mm*-*p*2*mm* is associated with a decrease of birefringence as indicated by the color change in the spherulitc domains (Figure S3h–j). Together with the large decrease of one lattice parameter from $a_{\mathrm{squ}} = 4.0$ nm to $b_{\mathrm{rec}} = 3.64$ nm, it is concluded that the cell size shrinkage takes place by tilting the OPE cores out of the crystallographic plane. According to $\beta = \cos^{-1}(b_{\mathrm{rec}}/L_{\mathrm{mol}})$ and assuming $L_{\mathrm{mol}} = 4.4$ nm, a tilt angle $\beta = 36°$ can be estimated. This strong tilt which is required for assuming an alternating donor–acceptor core packing reduces the space available in the rectangular cells too much and requires a simultaneous lattice expansion in the orthogonal direction. This leads to a slight elongation of a_{rec} from 4.0 to 4.15 nm in order to adjust the prismatic cell volume to the chain volume by an increasing orientational-order parameter of the rods. Because a smaller tilt than 36° is disfavored by the specific core–core interaction between the FOPEs [129], a simultaneous shrinkage of all honeycomb walls by retaining the square lattice (as found for **H9/6**; Figure S9g) and assuming a smaller tilt (= longitudinal shift) [97] is obviously not possible. Thus, retaining a nontilted organization in half of the walls and the emergence of a significant tilt in the other half is in line with the proposed restrictions of the intermolecular shift between the FOPE cores (Figure 10c,f)

It can be concluded that the rhomb tiling (*c*2*mm*) is replaced by a rectangular tiling (*p*2*mm*) if the spacer length m falls below a certain limit. Such result is also supported by the dV/dr curves in Figure 6, where *p*2*mm* exhibits a shorter tailing than *c*2*mm*. For longer spacers, a difference in space filling is easily compensated by modification of n_{wall} or angular deformation. However, this angular deformation is associated with the tightening of two of the four vertices, which is unfavorable for the packing of the bulky $-\mathrm{SiR}_3$ groups, especially if relatively short spacers restrict their possible arrangements. For these compounds, the transition to rectangular cells, retaining the 90° angles and reducing the space in the prismatic cells by tilting some molecules, becomes favorable.

4.4 | M-Phases

In both series, **H*m*/*n*** and **F*m*/*n*** there are additional birefringent mesophases with mosaic-like textures (M) all having yet unsolved complex SAXS patterns and occurring in small temperature ranges or as metastable phases within the steric frustration range associated with the triangle–square transition. At this cross-over, several periodic mixed triangle–square tilings and quasicrystalline dodecagonal tiling patterns are expected to occur [31, 130]. The discovery of an A15 tetrahedral rod-sphere packing at the triangle–square cross-over raises the question if there could be a cross-over between the dodecagonal quasicrystals representing sphere packings [131] and those derived from tessellations by polygonal prismatic cells [132–135], obviously competing with each other in the triangle–square frustration range. Whether these unknown intermediate phases represent alternative modes of Frank–Kasper-type networks combining spheres and rods, or complex honeycombs with super-tiling patterns combining different cell shapes, is the subject of ongoing work.

5 | Conclusion

Segmented network phases, recently predicted for block copolymers [136] and experimentally observed for rod-like bolapolyphiles having bulky side-chains [33–36], represent a new mode of soft self-assembly combining features of bicontinuous and micellar assemblies in a single structure, that is, they represent sphere (mesoatom) packings interconnected by struts forming the bonds between them. Among them, a Frank–Kasper-type segmented network phase consisting of tetrahedral rod-packing combined with spheres on a $Pm\bar{3}n$ lattice was found for rod-like bolapolyphiles with properly designed flexible side-chains (Figure 2c,e) [38, 94]. It occurs upon increasing side-chain

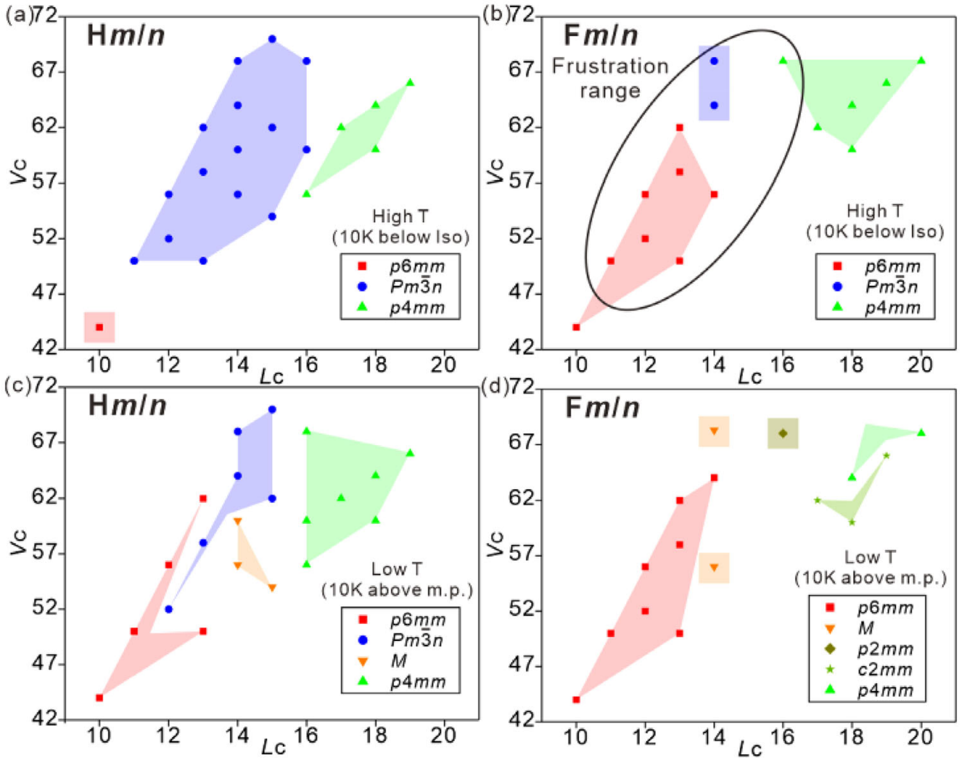

FIGURE 12 | 2D-plots of the phase ranges in the two series **H*m*/*n*** and **F*m*/*n*** depending on side-chain volume (V_C) and side-chain length (L_C).

length and volume as intermediate structure in the sequence Col$_{hex}$/$p6mm$ → Cub$_{net}$/$Pm\bar{3}n$ → Col$_{squ}$/$p4mm$ at the transition from triangular to square honeycombs (Figures 5, 7, and 12). It turned out that the side-chain length L_C and especially the length of the oligomethylene spacer m separating the bulky —SiR$_3$ units from the core, that is, the capability of distant space filling without entropically unfavorable chain stretching, represent the main parameters selecting the phase structure.

Broad ranges of the network-type A15 phase were found for compounds with a nonfluorinated OPE core, while for the core-fluorinated compounds, there is only a small molecular structural window for A15 phase formation (Figure 12). This is attributed to a destabilization by the mismatch between the required and available length of the bonds interconnecting the meso-atoms. While OPEs allows a continuous adjustment of the bond length by longitudinal shift of the polyaromatic rods with respect to each other (Figure 10, left side), for the FOPE cores, there are distinct energetic minima restricting the possible degrees of shift (Figure 10, right side), thus destabilizing the meso-atom bonds in the A15 phase and reducing its range of existence. This restriction in longitudinal shift also affects the organization of the core fluorinated molecules in the honeycomb walls and thus is responsible for the formation of either rhombic or rectangular honeycombs replacing the square honeycombs of some FOPE compounds at lower temperature.

Overall, the work highlights the effects of aggregation of π-conjugated rods on self-assembly in reticular LCs. It also provides clues for the rational design of related soft- and solid-state materials toward new and more complex architectures, eventually leading to still illusive quasiperiodic networks [137].

Acknowledgements

This work was supported by the Deutsche Forschungsgemeinschaft (436494874-RTG 2670), the National Natural Science Foundation of China (12204369), Science and Technology Agency of Shaanxi Province (2023-YBGY-459), and China Postdoctoral Science Foundation (2022M712551, 2023T160505). The authors are grateful to Beamline BL16B1 at SSRF (Shanghai Synchrotron Radiation Facility, China) for providing the beamtimes.

Conflicts of Interest

The authors declare no conflicts of interest.

Data Availability Statement

The data that support the findings of this study are available in the supplementary material of this article.

References

1. M. Kumar and S. Kumar, “Liquid Crystals in Photovoltaics: A New Generation of Organic Photovoltaics,” *Polymer Journal* 49 (2017): 85.

2. Y. Hong, J. W. Y. Lam, and B. Z. Tang, “Aggregation-Induced Emission,” *Chemical Society Reviews* 40 (2011): 5361.

3. L. H. Y. Liu, F. X. Lin, K. Fu, et al., “Highly Efficient Luminescent Liquid Crystal With Aggregation-Induced Energy Transfer,” *ACS Applied Materials & Interfaces* 11 (2019): 3516.

4. Y. Wu, M. Li, Z. G. Zheng, Z. Q. Yu, and W. H. Zhu, “Liquid Crystal Assembly for Ultra-Dissymmetric Circularly Polarized Luminescence and Beyond,” *Journal of the American Chemical Society* 145 (2023): 12951.

5. Z. L. Gong, X. Zhu, Z. Zhou, et al., “Frontiers in Circularly Polarized Luminescence: Molecular Design, Self-Assembly, Nanomaterials, and Applications,” *Science China Chemistry* 64 (2021): 2060.

6. J. Liu, Y. Molard, M. E. Prévot, and T. Hegmann, “Highly Tunable Circularly Polarized Emission of an Aggregation-Induced Emission Dye Using Helical Nano- and Microfilaments as Supramolecular Chiral Templates,” *ACS Applied Materials & Interfaces* 14 (2022): 2939.

7. Y. X. Hu, W. J. Li, P. P. Jia, X. Q. Wang, L. Xu, and H. B. Yang, “Supramolecular Artificial Light-Harvesting Systems with Aggregation-Induced Emission,” *Advanced Optical Materials* 8 (2020): 2000265.

8. M. R. Wasielewski, “Self-Assembly Strategies for Integrating Light Harvesting and Charge Separation in Artificial Photosynthetic Systems,” *Accounts of Chemical Research* 42 (2009): 1910–1921.

9. J. W. Goodby, J. P. Collings, T. Kato, and C. Tschierske, H. F. Gleeson, P. Raynes, eds., *Handbook of Liquid Crystals* (Weinheim: Wiley-VCH, 2014).

10. P. J. Collings and J. W. Goodby, *Introduction to Liquid Crystals: Chemistry and Physics* (Boca Raton, FL: CRC Press, 2019).

11. E.-K. Fleischmann and R. Zentel, “Liquid-Crystalline Ordering as a Concept in Materials Science: From Semiconductors to Stimuli-Responsive Devices,” *Angewandte Chemie International Edition* 52 (2013): 8810.

12. H. K. Bisoyi and Q. Li, “Liquid Crystals: Versatile Self-Organized Smart Soft Materials,” *Chemical Reviews* 122 (2022): 4887.

13. N. Koide, ed., *The Liquid Crystal Display Story* (Tokyo: Springer, 2014).

14. R. Iwai, H. Yoshida, Y. Arakawa, et al., “Near-Room-Temperature π-Conjugated Nematic Liquid Crystals in Molecules with a Flexible Seven-Membered Ring Structure,” *Aggregate* (2024): e660, https://doi.org/10.1002/agt2.660.

15. J. Uchida, B. Soberats, M. Gupta, and T. Kato, “Advanced Functional Liquid Crystals,” *Advanced Materials* 34 (2022): 2109063.

16. C. Tschierske, “Development of Structural Complexity by Liquid-Crystal Self-Assembly,” *Angewandte Chemie International Edition* 52 (2013): 8828.

17. C. Tschierske, “Liquid Crystal Engineering—New Complex Mesophase Structures and Their Relations to Polymer Morphologies, Nanoscale Patterning and Crystal Engineering,” *Chemical Society Reviews* 36 (2007): 1930.

18. C. Tschierske, C. Nürnberger, H. Ebert, et al., “Complex Tiling Patterns in Liquid Crystals,” *Interface Focus* 2 (2012): 669.

19. Z. He, X. Wang, P. Zhang, A. C. Shi, and K. Jiang, “Theory of Polygonal Phases Self-Assembled From T-Shaped Liquid Crystalline Molecules,” *Macromolecules* 57 (2024): 2154.

20. R. M. Fuoss and D. Edelson, “Bolaform Electrolytes. I. Di-(β-Trimethylammonium Ethyl) Succinate Dibromide and Related Compounds,” *Journal of the American Chemical Society* 73 (1951): 269.

21. G. A. Jeffrey and W. Saenger, *Hydrogen Bonding in Biological Structures* (Berlin: Springer, 1994).

22. E. G. Atovmyan, S. V. Koshchii, and T. N. Fedotova, “Investigation of Hydrogen Bonds in Alkyl Glycerol Ethers,” *Journal of Applied Spectroscopy* 48 (1988): 202.

23. J. S. Lomas, “Cooperativity in Alkane-1,2- and 1,3-Polyols: NMR, QTAIM, and IQA Study of O—H···OH and C—H···OH Bonding Interactions,” *Magnetic Resonance in Chemistry* 58 (2020): 666.

24. C. P. Brock, “Crystal Packing in Vicinal Diols $C_nH_m(OH)_2$,” *Acta Crystallographica Section B* 58 (2002): 1025.

25. R. Chelakkot, R. Lipowsky, and T. Gruhn, “Novel Low-Density Structure for Hard Rods with Adhesive End Groups,” *Macromolecules* 39 (2006): 7138.

26. T. D. Nguyen and S. C. Glotzer, “Reconfigurable Assemblies of Shape-Changing Nanorods,” *ACS Nano* 4 (2010): 2585.

27. S. Poppe, M. Poppe, H. Ebert, et al., “Effects of Lateral and Terminal Chains of X-Shaped Bolapolyphiles with Oligo(Phenylene Ethynylene) Cores on Self-Assembly Behaviour. Part 1: Transition Between Amphiphilic and Polyphilic Self-Assembly in the Bulk,” *Polymers* 9 (2017): 471.

28. R. Kieffer, M. Prehm, B. Glettner, et al., “X-Shaped Polyphilics: Liquid Crystal Honeycombs With Single-Molecule Walls,” *Chemical Communications* (2008): 3861.

29. A. Saeed, M. Poppe, M. B. Wagner, et al., “The Rhombic Honeycomb—A New Mode of Self-Assembly in Liquid Crystalline Soft Matter,” *Chemical Communications* 58 (2022): 7054.

30. M. Poppe, C. Chen, S. Poppe, C. Kerzig, F. Liu, and C. T. schiersk, “Different Modes of Deformation of Soft Triangular Honeycombs at the Sub-5 nm Scale,” *Advanced Materials* 32 (2020): 2005070.

31. B. Glettner, F. Liu, X. Zeng, et al., “Liquid-Crystalline Kagome,” *Angewandte Chemie International Edition* 47 (2008): 9063.

32. M. Poppe, C. Chen, S. Poppe, F. Liu, and C. Tschierske, “A Periodic Dodecagonal Supertiling by Self-Assembly of Star-Shaped Molecules in the Liquid Crystalline State,” *Communications Chemistry* 3 (2020): 70.

33. X. Cai, S. Hauche, S. Poppe, et al., “Network Phases With Multiple-Junction Geometries at the Gyroid–Diamond Transition,” *Journal of the American Chemical Society* 145 (2023): 1000.

34. X. Zeng, S. Poppe, A. Lehmann, et al., “A Self-Assembled Bicontinuous Cubic Phase With a Single-Diamond Network,” *Angewandte Chemie International Edition* 58 (2019): 7375.

35. S. Poppe, X. Cheng, C. Chen, et al., “Liquid Organic Frameworks: The Single-Network ‘Plumber’s Nightmare’ Bicontinuous Cubic Liquid Crystal,” *Journal of the American Chemical Society* 142 (2020): 3296.

36. C. Chen, M. Poppe, S. Poppe, C. Tschierske, and F. Liu, “Liquid Organic Frameworks: A Liquid Crystalline 8-Connected Network With Body-Centered Cubic Symmetry,” *Angewandte Chemie International Edition* 59 (2020): 20820.

37. Y. Sun and F. A. Escobedo, “Coarse-Grained Molecular Simulation of Bolapolyphiles With a Multident Lateral Chain: Formation and Structural Analysis of Cubic Network Phases,” *Journal of Chemical Theory and Computation* 20 (2024): 1519.

38. C. Chen, M. Poppe, S. Poppe, M. Wagner, C. Tschierske, and F. Liu, “Tetrahedral Liquid-Crystalline Networks: An A15-Like Frank–Kasper Phase Based on Rod-Packing,” *Angewandte Chemie International Edition* 61 (2022): e20220344.

39. F. C. Frank and J. S. Kasper, “Complex Alloy Structures Regarded as Sphere Packings. I. Definitions and Basic Principles,” *Acta Crystallographica* 11 (1958): 184.

40. F. C. Frank and J. S. Kasper, “Complex Alloy Structures Regarded as Sphere Packings. II. Analysis and Classification of Representative Structures,” *Acta Crystallographica* 12 (1959): 483.

41. X.-Y. Liu, X.-Y. Yan, Y. Liu, et al., “Self-Assembled Soft Alloy With Frank–Kasper Phases Beyond Metals,” *Nature Materials* 23 (2024): 570.

42. X.-H. Li,, X. Kuang, X. Y. Liu, et al., “Exploring Fullerene-Based Superlattices Self-Assembled via Giant Molecules,” *Giant* 16 (2023): 100196.

43. G. R. Stewart, “Superconductivity in the A15 Structure,” *Physica C* 514 (2015): 28.

44. K. Fontell, “Cubic Phases in Surfactant and Surfactant-Like Lipid Systems,” *Colloid and Polymer Science* 268 (1990): 264.

45. R. R. Balmbra, J. S. Clunie, and J. F. Goodman, “Cubic Mesomorphic Phases,” *Nature* 222 (1969): 1159–1160.

46. V. Luzzati, R. Vargas, P. Mariani, A. Gulik, and H. Delacroix, “Cubic Phases of Lipid-Containing Systems,” *Journal of Molecular Biology* 229 (1993): 540.

47. A. Jayaraman and M. K. Mahanthappa, “Counterion-Dependent Access to Low-Symmetry Lyotropic Sphere Packings of Ionic Surfactant Micelles,” *Langmuir* 34 (2018): 2290.

48. K. Borisch, S. Diele, P. Göring, and C. Tschierske, “Molecular Design of Amphitropic Liquid Crystalline Carbohydrates–Amphiphilic N-Methyl-Glucamides Exhibiting Lamellar, Columnar or Cubic Mesophases,” *Chemical Communications* (1996): 237.

49. K. Borisch, S. Diele, P. Göring, H. Kresse, and C. Tschierske, “Design of Thermotropic Liquid Crystals With Micellar Cubic Mesophases: Amphiphilic *N*-(2,3-Dihydroxypropyl)Benzamides,” *Angewandte Chemie International Edition* 36 (1997): 2087.

50. M. Huang, C.-H. Hsu, J. Wang, et al., “Selective Assemblies of Giant Tetrahedra via Precisely Controlled Positional Interactions,” *Science* 348 (2015): 424.

51. V. S. K. Balagurusamy, G. Ungar, V. Percec, and G. Johansson, “Rational Design of the First Spherical Supramolecular Dendrimers Self-Organized in a Novel Thermotropic Cubic Liquid-Crystalline Phase and the Determination of Their Shape by X-Ray Analysis,” *Journal of the American Chemical Society* 119 (1997): 1539.

52. H.-J. Sun, S. Zhang, and V. Percec, “From Structure to Function via Complex Supramolecular Dendrimer Systems,” *Chemical Society Reviews* 44 (2015): 3900.

53. X. H. Cheng, K. Das, S. Diele, and C. Tschierske, “Influence of Semiperfluorinated Chains on the Liquid Crystalline Properties of Amphiphilic Polyols: Novel Materials With Thermotropic Lamellar, Columnar, Bicontinuous Cubic, and Micellar Cubic Mesophases,” *Langmuir* 18 (2002): 6521.

54. T. Jun, H. Park, S. Jeon, et al., “Mesoscale Frank–Kasper Crystal Structures From Dendron Assembly by Controlling Core Apex Interactions,” *Journal of the American Chemical Society* 143 (2021): 17548.

55. B.-K. Cho, “Spontaneous Bulk Organization of Molecular Assemblers Based on Aliphatic Polyether and/or Poly(Benzyl Ether) Dendrons,” *Polymer Journal* 44 (2012): 475.

56. S. Yazaki, Y. Kamikawa, M. Yoshio, et al., “Ionic Liquid Crystals: Self-assembly of Imidazolium Salts Containing an L-Glutamic Acid Moiety,” *Chemistry Letters* 37 (2008): 538.

57. T. Noguchi, K. Kishikawa, and S. Kohmoto, “Tailoring of Ionic Supramolecular Assemblies Based on Ammonium Carboxylates Toward Liquid-Crystalline Micellar Cubic Mesophases,” *Liquid Crystals* 35 (2008): 1043.

58. X. H. Cheng, S. Diele, and C. Tschierske, “Molecular Design of Liquid-Crystalline Block Molecules: Semifluorinated Pentaerythritol Tetrabenzoates Exhibiting Lamellar, Columnar, and Cubic Mesophases,” *Angewandte Chemie International Edition* 39 (2000): 592.

59. C. M. Wentz, K. K. Lachmayr, E. H. R. Tsai, and L. R. Sita, “Rapid Phase Transitions of Thermotropic Glycolipid Quasicrystal and Frank-Kasper Mesophases: A Mechanistic Rosetta Stone,” *Angewandte Chemie International Edition* 62 (2023): e202302739.

60. I. Bury, B. Heinrich, C. Bourgogne, D. Guillon, and B. Donnio, “Supramolecular Self-Organization of ‘Janus-Like’ Diblock Codendrimers: Synthesis, Thermal Behavior, and Phase Structure Modeling,” *Chemistry: A European Journal* 12 (2006): 8396.

61. A. Kohlmeier and D. Janietz, “Mesomorphic Block Molecules: Semiperfluorinated 1,3,5-Triazine Derivatives Exhibiting Lamellar, Columnar, and Cubic Mesophases,” *Chemistry of Materials* 18 (2006): 1483.

62. N. Komiyama, T. Ohkubo, Y. Maeda, et al., “Magnetic Supramolecular Spherical Arrays: Direct Formation of Micellar Cubic Mesophase by Lanthanide Metallomesogens With 7-Coordination Geometry,” *Advancement of Science* 11 (2024): 2309226.

63. D. Sahoo, M. Peterca, M. R. Imam, B. E. Partridge, Q. Xiao, and V. Percec, “Conformationally Flexible Dendronized Cyclotetraveratrylenes (CTTV)s Self-organize a Large Diversity of Chiral Columnar, Frank-Kasper and Quasicrystal Phases,” *Giant* 10 (2022): 100096.

64. T. Hatano and T. Kato, “A Columnar Liquid Crystal Based on Triphenylphosphine Oxide—Its Structural Changes Upon Interaction With Alkaline Metal Cations,” *Chemical Communications* 2006 (2006): 1277.

65. Y. Sagara and T. Kato, “Stimuli-Responsive Luminescent Liquid Crystals: Change of Photoluminescent Colors Triggered by a Shear-Induced Phase Transition,” *Angewandte Chemie International Edition* 47 (2008): 5175.

66. H. Mukai, M. Yokokawa, M. Ichihara, and K. Hatsusaka, “Discotic Liquid Crystals of Transition Metal Complexes 42: The Detailed Phase Structures and Phase Transition Mechanisms of Two Cub Mesophases Shown by Discotic Liquid Crystals Based on Phthalocyanine Metal Complexes,” *Journal of Porphyrins and Phthalocyanines* 14 (2010): 188–197.

67. V. Percec, M. R. Imam, M. Peterca, et al., “Self-Assembly of Dendronized Triphenylenes Into Helical Pyramidal Columns and Chiral Spheres,” *Journal of the American Chemical Society* 131 (2009): 7662–7677.

68. M. R. Imam, M. Peterca, Q. Xiao, and V. Percec, “Enhancing Conformational Flexibility of Dendronized Triphenylene via Diethylene Glycol Linkers Lowers Transitions of Helical Columnar, Frank-Kasper, and Quasicrystal Phases,” *Giant* 10 (2022): 100098.

69. J. Huang, Z. Su, M. Huang, et al., “Spherical Supramolecular Structures Constructed via Chemically Symmetric Perylene Bisimides: Beyond Columnar Assembly,” *Angewandte Chemie International Edition* 59 (2020): 18563–18571.

70. B. M. Rosen, D. A. Wilson, C. J. Wilson, et al., “Predicting the Structure of Supramolecular Dendrimers via the Analysis of Libraries of AB_3 and Constitutional Isomeric AB_2 Biphenylpropyl Ether Self-Assembling Dendrons,” *Journal of the American Chemical Society* 131 (2009): 17500–17521.

71. X. Liu, R. Zhang, Y. Shao, et al., “Crowding-Induced Unconventional Phase Behaviors in Dendritic Rodlike Molecules via Side-Chain Engineering,” *ACS Macro Letters* 10 (2021): 844–850.

72. C.-J. Jang, J.-H. Ryu, J.-D. Lee, D. Sohn, and M. Lee, “Synthesis and Supramolecular Nanostructure of Amphiphilic Rigid Aromatic-Flexible Dendritic Block Molecules,” *Chemistry of Materials* 16 (2004): 4226.

73. X. Cheng, X. Bai, S. Jing, H. Ebert, M. Prehm, and C. Tschierske, “Self-Assembly of Imidazolium-Based Rodlike Ionic Liquid Crystals: Transition From Lamellar to Micellar Organization,” *Chemistry: A European Journal* 16 (2010): 4588–4601.

74. S. H. Seo, J. H. Park, G. N. Tew, and J. Y. Chang, “Thermotropic Liquid Crystals of ^{1}H-Imidazole Amphiphiles Showing Hexagonal Columnar and Micellar Cubic Phases,” *Tetrahedron Letters* 48 (2007): 6839–6844.

75. X. Tan, L. Kong, H. Dai, X. Cheng, F. Liu, and C. Tschierske, “Triblock Polyphiles Through Click Chemistry: Self-Assembled Thermotropic Cubic Phases Formed by Micellar and Monolayer Vesicular Aggregates,” *Chemistry: A European Journal* 19 (2013): 16303.

76. T. Yasuda, H. Ooi, J. Morita, et al., “π-Conjugated Oligothiophene-Based Polycatenar Liquid Crystals: Self-Organization and Photoconductive, Luminescent, and Redox Properties,” *Advanced Functional Materials* 19 (2009): 411.

77. T. Hatano and T. Kato, “Nanostructured Columnar and Cubic Liquid-Crystalline Assemblies Consisting of Unconventional Rigid Mesogens Based on Triphenylmethanes,” *Tetrahedron* 64 (2008): 8368.

78. X. Feng, R. Zhang, Y. Li, et al., “Hierarchical Self-Organization of AB n Dendron-Like Molecules Into a Supramolecular Lattice Sequence,” *ACS Central Science* 3 (2017): 860.

79. S. Lee, C. Leighton, and F. S. Bates, “Sphericity and Symmetry Breaking in the Formation of Frank–Kasper Phases From One Component Materials,” *Proceedings National Academy of Science of the United States of America* 111 (2014): 17723.

80. A. Reddy, M. B. Buckley, A. Arora, F. S. Bates, K. D. Dorfman, and G. M. Grason, “Stable Frank–Kasper Phases of Self-Assembled, Soft Matter Spheres,” *Proceedings National Academy of Science of the United States of America* 115 (2018): 10233.

81. K. D. Dorfman, “Frank–Kasper Phases in Block Polymers,” *Macromolecules* 54 (2021): 10251.

82. K. Kim, M. W. Schulze, A. Arora, et al., “Thermal Processing of Diblock Copolymer Melts Mimics Metallurgy,” *Science* 356 (2017): 520.

83. Z. Xu, Q. Dong, and W. Li, “Architectural Design of Block Copolymers,” *Macromolecules* 57 (2024): 1869.

84. P. Ziherl and R. D. Kamien, “Maximizing Entropy by Minimizing Area: Towards a New Principle of Self-Organization,” *Journal of Physical Chemistry B* 105 (2001): 10147.

85. H. Lee, J. Kim, and M. J. Park, “Exploration of Complex Nanostructures in Block Copolymers,” *Physical Review Materials* 8 (2024): 020302.

86. D. A. Tomalia and S. N. Khanna, “A Systematic Framework and Nanoperiodic Concept for Unifying Nanoscience: Hard/Soft Nanoelements, Superatoms, Meta-Atoms, New Emerging Properties, Periodic Property Patterns, and Predictive Mendeleev-Like Nanoperiodic Tables,” *Chemical Reviews* 116 (2016): 2705.

87. G. M. Grason and E. L. Thomas, “How Does Your Gyroid Grow? A Mesoatomic Perspective on Supramolecular, Soft Matter Network Crystals,” *Physical Review Materials* 7 (2023): 045603.

88. X.-Y. Yan, Y. Liu, X.-Y. Liu, et al., “Guidelines for Superlattice Engineering With Giant Molecules: The Pivotal Role of Mesoatoms,” *Physical Review Materials* 7 (2023): 120302.

89. Y. Liu, Q.-Y. Guo, Z. Huang, et al., “Mesoatomic Engineering for Programmable Spherical Packing Superlattices in Self-Assembly of Giant Molecular Clusters,” *CCS Chemistry* (2024), https://doi.org/10.31635/ccschem.024.202404791.

90. S. Wang, S. Lee, J. S. Du, et al., “The Emergence of Valency in Colloidal Crystals Through Electron Equivalents,” *Nature Materials* 21 (2022): 580.

91. O. M. Yaghi, M. O’Keeffe, N. W. Ockwig, H. K. Chae, M. Eddaoudi, and J. Kim, “Reticular Synthesis and the Design of New Materials,” *Nature* 423 (2003): 705.

92. U. H. F. Bunz, “Poly(aryleneethynylene)s,” *Macromolecular Rapid Communications* 30 (2009): 772.

93. A. Kreyes, A. Masoud, I. Lieberwirth, et al., “The Longest β-Unsubstituted Oligothiophenes and Their Self-Assembly in Solution,” *Chemistry of Materials* 22 (2010): 6453.

94. C. Anders, M. Wagner, M. Alaasar, et al., “Highly Branched Bolapolyphilic Liquid Crystals With a Cubic A15 Network at the Triangle-Square Transition,” *Chemical Communications* 60 (2024): 1023.

95. M. Hird, “Fluorinated Liquid Crystals—Properties and Applications,” *Chemical Society Reviews* 36 (2007): 2070.

96. M. Poppe, C. Chen, H. Ebert, et al., “Transition From Nematic to Gyroid-Type Cubic Soft Self-Assembly by Side-Chain Engineering of π-Conjugated Sticky Rods,” *Soft Matter* 13 (2017): 4381.

97. M. Poppe, C. Chen, F. Liu, M. Prehm, S. Poppe, and C. Tschiersk, “Emergence of Tilt in Square Honeycomb Liquid Crystalse,” *Soft Matter* 13 (2017): 4676.

98. M. Poppe, C. Chen, F. Liu, S. Poppe, and C. Tschierske, “Emergence of Uniform Tilt and π-Stacking in Triangular Liquid Crystalline Honeycombs,” *Chemical Communications* 57 (2021): 6526.

99. S. Werner, H. Ebert, B.-D. Lechner, et al., “Dendritic Domains With Hexagonal Symmetry Formed by X-Shaped Bolapolyphiles in Lipid Membranes,” *Chemistry: A European Journal* 21 (2015): 8840.

100. M. Poppe, C. Chen, F. Liu, S. Poppe, and C. Tschierske, “Formation of a Cubic Liquid Crystalline Nanostructure With π-Conjugated Fluorinated Rods on the Gyroid Minimal Surface,” *Chemistry: A European Journal* 23 (2017): 7196.

101. K. Sonogashira, Y. Tohda, and N. Hagihara, “A Convenient Synthesis of Acetylenes: Catalytic Substitutions of Acetylenic Hydrogen With Bromoalkenes, Iodoarenes and Bromopyridines,” *Tetrahedron Letters* 16 (1975): 4467.

102. Y. C. Chiang, H. C. Wu, H.-F. Wen, et al., “Tailoring Carbosilane Side Chains Toward Intrinsically Stretchable Semiconducting Polymers,” *Macromolecules* 52 (2019): 4396.

103. Y. Duan, J. H. Lin, J. C. Xiao, and Y. C. Gu, “Fe-Catalyzed insertion of Fluoromethylcarbenes Generated From Sulfonium Salts Into X–H bonds (X = Si, C, P),” *Organic Chemistry Frontiers* 4 (2017): 1917–1920.

104. G. Nagarjuna, A. Kokil, J. Kumar, and D. Venkataraman, “A Straightforward Route to Electron Transporting Conjugated Polymers,” *Journal of Materials Chemistry* 22 (2012): 16091.

105. R. van Rijsbergen, M. J. O. Anteunis, and A. De Bruyn, “Selective Removal of the Isopropylidene Group in 4-*O*-Protected 1,6-Anhydro-2,3-*O*-Isopropylidene-β-D-Mannopyranose and the Conformational Impact of It,” *Journal of Carbohydrate Chemistry* 2 (1983): 395.

106. A. Immirzi and B. Perini, “Prediction of Density in Organic Crystals,” *Acta Crystallographica Section A* 33 (1977): 216.

107. C. Tschierske, *Topics in Current Chemistry* (Berlin, Heidelberg: Springer, 2012).

108. Y. Xu, Y. Hu, Q. Chen, and J. Wen, “Synthesis and Characterization of Octafluorinated 1,2-(4,4′-Dialkoxyaryl)Acetylene Monomers and 1,4-Bis[(4′,4′-Dialkoxyphenyl)Ethynyl]Benzene Dimers,” *Journal of Materials Chemistry* 5 (1995): 219.

109. G. N. Patwari, P. Venuvanalingam, and M. Kolaski, “Phenylacetylene Dimer: Ab Initio and DFT Study,” *Chemical Physics* 415 (2013): 150.

110. S. E. Wheeler and K. N. Houk, “Origin of Substituent Effects in Edge-to-Face Aryl–Aryl Interactions,” *Molecular Physics* 107 (2009): 749.

111. P. V. James, P. K. Sudeep, C. H. Suresh, and K. G. Thomas, “Photophysical and Theoretical Investigations of Oligo(p-Phenyleneethynylene)s: Effect of Alkoxy Substitution and Alkyne−Aryl Bond Rotations,” *Journal of Physical Chemistry A* 110 (2006): 4329.

112. M. Levitus, K. Schmieder, H. Ricks, K. D. Shimizu, U. H. F. Bunz, and M. A. Garcia-Garibay, “Steps To Demarcate the Effects of Chromophore Aggregation and Planarization in Poly(Phenyleneethynylene)s. 1. Rotationally Interrupted Conjugation in the Excited States of 1,4-Bis(Phenylethynyl)Benzene,” *Journal of the American Chemical Society* 123 (2001): 4259.

113. C. A. Hunter and J. K. M. Sanders, “The Nature of .pi.-.pi. interactions,” *Journal of the American Chemical Society* 112 (1990): 5525.

114. S. E. Wheeler, “Understanding Substituent Effects in Noncovalent Interactions Involving Aromatic Rings,” *Accounts of Chemical Research* 46 (2013): 1029.

115. K. Carter-Fenk and J. M. Herbert, “Reinterpreting π-Stacking,” *Physical Chemistry Chemical Physics* 22 (2020): 24870.

116. K. Kishikawa, “Utilization of the Perfluoroarene-Arene Interaction for Stabilization of Liquid Crystal Phases,” *Isrrael Journal of Chemistry* 52 (2012): 800.

117. K. Kishikawa, S. Aikyo, S. Akiyama, et al., “Realization of a Lateral Directional Order in Nematic and Smectic A Phases of Rodlike Molecules by Using Perfluoroarene–Arene Interactions,” *Soft Matter* 7 (2011): 5176.

118. A. Kundu, S. Sen, and G. N. Patwari, “Dipole Moment Propels π-Stacking of Heterodimers of Fluorophenylacetylenes,” *Journal of Physical Chemistry* 124 (2020): 7470.

119. S. Yamada, M. Morita, T. Agou, T. Kubota, T. Ichikawa, and T. Konno, “Thermoresponsive Luminescence Properties of Polyfluorinated Bistolane-Type Light-Emitting Liquid Crystals,” *Organic & Biomolecular Chemistry* 16 (2018): 5609.

120. G. W. Coates, A. R. Dunn, L. M. Henling, D. A. Dougherty, and R. H. Grubbs, “Phenyl–Perfluorophenyl Stacking Interactions: A New Strategy for Supermolecule Construction,” *Angewandte Chemie International Edition* 36 (1997): 248.

121. S. A. Sharber, R. N. Baral, F. Frausto, T. E. Haas, P. Müller, and S. W. Thomas III, “Substituent Effects That Control Conjugated

Oligomer Conformation Through Non-Covalent Interactions," *Journal of the American Chemical Society* 139 (2017): 5164.

122. C. Dai, P. Nguyen, T. B. Marder, A. J. Scott, W. Clegg, and C. Viney, "Control of Single Crystal Structure and Liquid Crystal Phase Behaviour via Arene–Perfluoroarene Interactions," *Chemical Communications* (1999): 2493.

123. C. E. Smith, P. S. Smith, R. L. Thomas, et al., "Arene-Perfluoroarene Interactions in Crystal Engineering: Structural Preferences in Polyfluorinated Tolans," *Journal of Materials Chemistry* 14 (2004): 413.

124. K. B. Woody, J. E. Bullock, S. R. Parkin, and M. D. Watson, "Alternating Arene–Perfluoroarene Poly(Phenylene Ethynylenes)," *Macromolecules* 40 (2007): 4470.

125. L. Shua and M. Mayor, "Shape-Persistent Macrocycle With a Self-Complementary Recognition Pattern Based on Diacetylene-Linked Alternating Hexylbenzene and Perfluorobenzene Rings," *Chemical Communications* 2006 (2006): 4134.

126. S. Yamada and T. Konno, "Development of Donor-π-Acceptor-Type Fluorinated Tolanes as Compact Condensed Phase Luminophores and Applications in Photoluminescent Liquid-Crystalline Molecules," *Chemical Record* 23 (2023): e202300094.

127. A. Lehmann, A. Scholte, M. Prehm, et al., "Soft Rectangular Sub-5 nm Tiling Patterns by Liquid Crystalline Self-Assembly of T-Shaped Bolapolyphiles," *Advanced Functional Materials* 28 (2018): 1804162.

128. S. Poppe, A. Lehmann, M. Steimecke, et al., "Reticular Liquid Crystal Design: Controlling Complex Self-assembly of p-Terphenyl Rods by Side-Chain Engineering and Chirality," *Giant* 18 (2024): 100254.

129. C. Anders, V. M. Fischer, T. Tan, et al., "Modifying the Liquid Crystalline Chessboard Tilig-Soft Reticular Self-Assembly of Side-Chain Fluorinated Polyphiles," *Journal of Materials Chemistry C* (2025), https://doi.org/10.1039/D4TC04076G.

130. P. A. Stampfli, "A Dodecagonal Quasiperiodic Lattice in Two Dimensions," *Helvetica Physica Acta* 59 (1986): 1260.

131. X. Zeng, G. Ungar, Y. Liu, V. Percec, A. E. Dulcey, and J. K. Hobbs, "Supramolecular Dendritic Liquid Quasicrystals," *Nature* 428 (2004): 157.

132. K. Hayashida, T. Dotera, A. Takano, and Y. Matsushita, "Polymeric Quasicrystal: Mesoscopic Quasicrystalline Tiling in ABC Star Polymers," *Physical Review Letter* 98 (2007): 195502.

133. X. Zeng, B. Glettner, U. Baumeister, et al., "A Columnar Liquid Quasicrystal With a Honeycomb Structure That Consists of Triangular, Square and Trapezoidal Cells," *Nature Chemistry* 15 (2023): 625.

134. Y. Cao, A. Scholte, M. Prehm, et al., "Understanding the Role of Trapezoids in Honeycomb Self-Assembly—Pathways Between a Columnar Liquid Quasicrystal and Its Liquid-Crystalline Approximants," *Angewandte Chemie International Edition* 63 (2023): e202314454.

135. M. Imperor-Clerc, P. Kalugin, S. Schenk, W. Widdra, and S. Förster, "Higher-Dimensional Geometrical Approach for the Characterization of Two-Dimensional Square-Triangle-Rhombus Tilings," *Physical Review B* 110 (2024): 144106.

136. L. Li, Q. Dong, and W. Li, "Stabilize Various Novel Network Structures via the Alternate Arrangement of A/C Domains in Close Contact by Tailoring ABC Miktoarm Star Architectures," *Macromolecules* 57 (2023): 409.

137. J. J. Oppenheim, G. Skorupskii, and M. Dinca, "Aperiodic Metal–Organic Frameworks," *Chemical Science* 11 (2020): 11094.

Supporting Information

Additional supporting information can be found online in the Supporting Information section.